The Dissertation Committee for Andrew David Zimbroff certifies that this is the approved version of the following dissertation:

Occlusion of the Left Atrial Appendage Using Catheter-Delivered Hydrogels for Prevention of Thromboembolic Phenomena

Committee:

_____
Joseph J. Beaman, Supervisor

_____
Carlos Hidrovo

_____
F. Javier Otero

_____
Krishnendu Roy

_____
Carolyn Seepersad

Occlusion of the Left Atrial Appendage Using Catheter-Delivered Hydrogels for Prevention of Thromboembolic Phenomena

by

Andrew David Zimbroff, B.S.; M.S.

Dissertation

Presented to the Faculty of the Graduate School of

The University of Texas at Austin

in Partial Fulfillment

of the Requirements

for the Degree of

Doctor of Philosophy

The University of Texas at Austin

August 2013

Dedicated to my family, for being a constant and amazing source of support in too many ways to mention.

Acknowledgements

I would like to thank Dr. Joseph Beaman for being a supportive and helpful advisor. I cannot express how much I learned as his advisee, and how grateful I am for the opportunity to work with him. Without his guidance, this research would not have been possible, and I am incredibly grateful to have him as a mentor. Additionally, I would like to express gratitude to the rest of my dissertation committee. During the course of this research, there were many times when I got stuck or confused, and their guidance always helped get me back on track.

There were numerous graduate students and other collaborators that helped with this research in critical ways. Before starting this work, I knew almost nothing about hydrogels. Pallab was very patient, and answered all my questions I had on this topic. He also provided multiple material samples for testing and experimentation, without which, this research couldn't be completed. While working on mixing chamber analysis, I was fortunate to have the opportunity to collaborate with Dan and Ronit. Their contributions to this research were extremely valuable, and helped determine a successful mixing chamber design. Finally, I would like to acknowledge lab mates Felipe, Cameron, and Vikram, who were always willing to help, serving as an intelligent, outside perspective about questions I might have regarding this work.

Experimentation was a large part of this dissertation, and probably the largest hurdle I faced during my research. There were many people that immensely

helpful with gathering materials for testing, Richard and Joe were instrumental in getting catheters needed for balloon experimentation. Dr. Otero was also helpful in providing additional medical equipment for testing. Finally, Rosalie answered far too many of my questions regarding purchasing, the lab credit card, as well as the whereabouts of Dr. Beaman when needed.

It is also important to acknowledge everyone that was helpful and supportive in non-academic ways. I am grateful to everyone I met in Laurel and Taos coops, for contributing to a wonderful living environment for three and a half years. I am also appreciative of my current roommates, Aiko and Saaket. In addition, I am appreciative of everyone I worked with through 3Day Startup and Texas Venture Labs, for helping an intellectually stimulating environment outside of my dissertation work.

Finally, I am eternally grateful for all the love and support my family has given me. For as long as I can remember, they have served as a consistent source of encouragement, and have supported me through any endeavor I have undertaken. I only hope that I can one day give back as much to them as they have given me.

Andrew Zimbroff
The University of Texas at Austin
August 2013

Occlusion of the Left Atrial Appendage Using Catheter-Delivered Hydrogels for Prevention of Thromboembolic Phenomena

Andrew David Zimbroff, Ph.D.

The University of Texas at Austin, 2013

Supervisor Joseph J. Beaman

The Left Atrial Appendage, once thought to be "a relatively insignificant portion of cardiac anatomy," has currently been realized to possess "important pathological associations [1a]" particularly in its role in promoting serious, frequent thromboembolic events common in individuals suffering from Atrial Fibrillation. Prior approaches to mitigating these events have either required invasive procedures, proved less than fully effective, or presented with problematic sequelae of their own. This work will present a new procedure that addresses both the prevention of the thromboembolic events and the correction of the shortcomings of the major prior methods utilized.

A compliant hydrogel that can conform to the geometry of the appendage is proposed as a more effective method of occluding the chamber. This material would

be transported to the LAA in liquid form via a multi-lumen catheter, and then solidify within the chamber to form a solid plug. Previous research has identified a candidate hydrogel, comprised of PEG-tetra-thiol and Dextran vinyl sulfone as a candidate hydrogel for this application. Experimental work has investigated fluid properties of the material, as well as degradation and swelling properties of the material. Results from this experimentation were used for fluid transport analysis, and for evaluation of anchoring force of the hydrogel within the chamber.

Finally, subfunctions of the occlusion procedure were modeled and tested. During the actual procedure, a catheter balloon will isolate the appendage from the rest of the heart. A model was developed to study interactions between the appendage and this balloon. Additionally, due to fast solidification time, hydrogel components in the surgical procedure will be mixed in a mixing chamber at the tip of the catheter. Potential mixing chamber designs were modeled, and a ternary diffusion model was developed to better understand hydrogel mixing. Prototypes for both these subfunctions were built and tested as well. Additional analysis looked at the overall occlusion procedure, and how various subfunctions interacted with each other.

Table of Contents

List of Figures

List of Tables

Chapter 1: Introduction

The Left Atrial Appendage (LAA)

The Left Atrial Appendage or LAA is a structure, remnant of early embryonic development, that remains as a hooked, tubular muscular, pouch-like entity, with a narrow junction opening to the left atrium, yet clearly distinct structurally and physiologically from the Left Atrium (LA) proper. It lies within the pericardium, closely related in placement and function to the free wall of the left ventricle and its activity. It is trabeculated in appearance, demonstrating parallel muscle bars. It serves as a reservoir for circulating blood, particularly in conditions of imperfectly regulated flow -- one that can mediate blood pressure and create decompression when LA pressure is high. Related to these positive functional characteristics, the LAA has also been demonstrated to be the site in which thrombi have a strong predilection to occur, particularly in patients suffering from Atrial Fibrillation (AF) and/or to a lesser degree in mitral valve disease, as well as other cardiac pathology. The pathogenesis of thrombus formation in the LAA has mostly been studied in relation to AF, and the most common pathway of the occurrence has been the relative stasis of blood flow that occurs in the LAA as a result of its structure. Thrombus formations related to stagnation in the LAA has been determined to "represent the main source of disabling cardioembolic ischemic strokes in patients with AF" (ACC Guidelines, p. 24). Interestingly, not only *during* atrial fibrillation, but also *after* cardioversion (conversion to normal sinus rhythm electrically,

pharmacologically, spontaneously, or surgically), there may be thromboembolic events occurring within the first 3 and up to 10 days, and anticoagulation (which will be discussed later) is thus recommended after these procedures [1a].

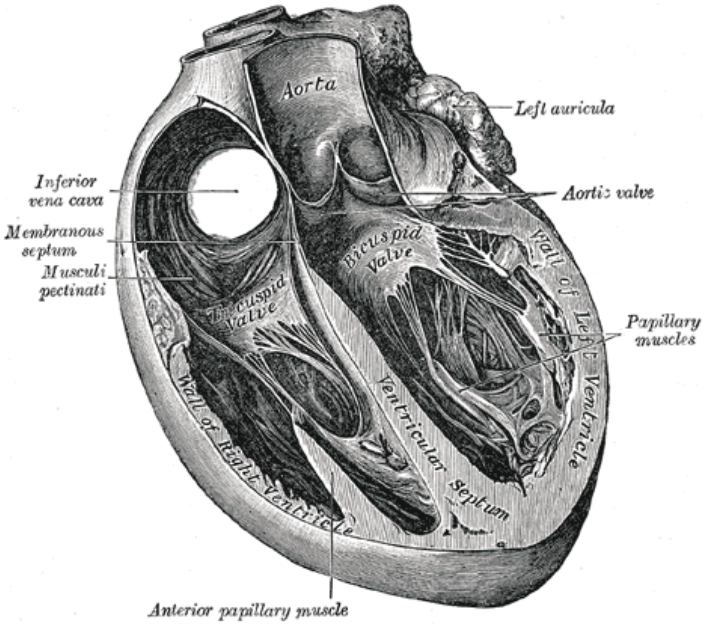

Figure 1.1: Diagram of the heart, with LAA labeled upper right (labeled as Left Auricula) [1b]

Atrial Fibrillation

Atrial Fibrillation is the most common sustained, cardiac arrhythmia (accounting for about one third of hospitalizations for cardiac rhythm pathology), causing an irregular heart rhythm in the upper chambers of the heart (See diagram of EKG). In this condition, the atria beat irregularly and out of sync with the lower chambers. This irregularity can cause the atria to beat more rapidly. Additionally, blood is not pumped completely, leading to pooling in the Left Atrium (LA) and Left Atrial Appendage (LAA), stasis that can result in thromboembolic events. These

thromboembolic events, (as well as other cardiovascular sequelae), can result in significant degrees of morbidity and mortality [1c].

The rate of ischemic stroke found in patients with AF without valve pathology averages 5% to 7% (7%, that is, if minor events are included) per year, which is 2 to 7 times that of patients without AF (reference # 23 in ACC article #1). This rate rises even higher if the patients with AF possess other risk factors for thromboembolic phenomena (e.g. hypertension). Some studies estimate that 35% of patients with untreated AF will have a stroke sometime in their lifetimes [1d]. In a further piece of evidence underlining the pivotal role of the LAA in thromboembolic phenomena associated with AF, one study demonstrated that as high as 95% of thrombi in patients with non-valve-related AF were shown to be localized to and/or originate in the LAA [1c 1d].

Figure 1.2: ElectroCardiogram of AF (top) and normal heart rhythm (bottom). The purple arrow points to a P-wave that is typically lost with AF

Treatment Methods

Multiple treatment methods are currently used to address clotting and resultant strokes caused by AF and located to a large extend in the LAA. The most common method of treatment is the use of oral anti-coagulation drugs. Warfarin (also known as Coumadin) is most common, and ~65% of patients with atrial fibrillation are treated with the medication at some point. These anticoagulants are not without complications, however. Hemorrhaging is the most significant side effect, and the medication can cause significant bleeding risks, particularly in cases where there is a risk of hemorrhagic stroke, a past history of bleeding, such as gastrointestinal bleeding, and a risk of history of falls. Other contraindications include end-stage liver disease, dialysis-dependent renal disease, uncontrolled hypertension, alcohol abuse, and a history of noncompliance with medical testing. Additionally, the drug exhibits multiple interactions with certain foods and other medications. As a result, fewer than 50% of patients, on average, eligible for long-term Warfarin therapy (studies vary from 21% to 67%) end up being treated with this method on a long-term basis [1e].

Ligation or complete amputation of the LAA has also been used to prevent clotting occurring in this structure and the resultant thromboembolic phenomena. It has been found that complete resection is really the only 100% effective means of excluding the LAA from all circulation. Less complicated ligature and suture techniques fail in 36% to 60% of patients, allowing for ongoing thromboembolic

risks. The complete amputation open-heart procedure entails using sutures or a clamp to close the opening of the appendage, and excising tissue. While this technique is effective at reducing clotting and strokes, it entails a long, costly procedure and certain instances of bleeding from delicate left atrial tissue. Some newer procedures have utilized some safer easier methods of resection that also utilize pericardium reinforcement. Still, considering the severity of the intervention, complete amputation is often not selected as a treatment method unless another cardiac surgical procedure (e.g. cardiopulmonary bias) is necessary and being done simultaneously [1d 1f].

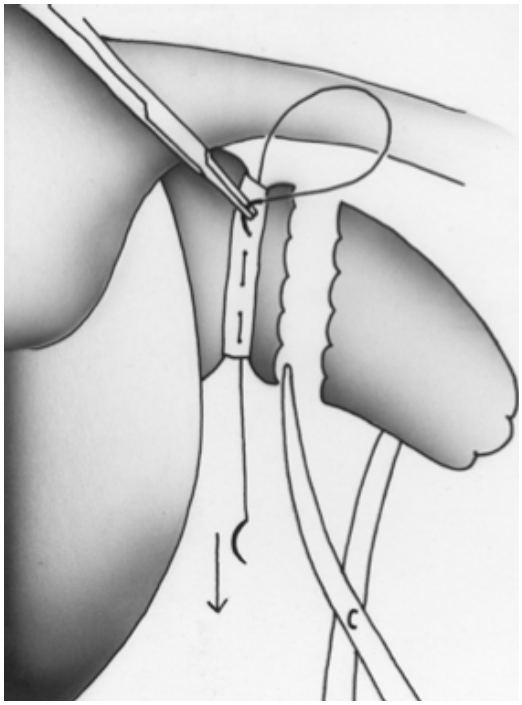

Figure 1.3 Amputation procedure for LAA [1f]

A less interventive treatment technique involves implanting of physical plugs. Physical plugs have been used with limited success. These plugs are

deployed via catheter, and they typically involve a far less complex procedure for deployment than the amputation procedure described above. The Watchman is currently the most used physical plug for LAA occlusion. This cardiac plug consists of a self-expanding frame made of braided Nitinol wires covered with polyester fabric. The device is transported to the LAA via catheter in a folded state, and unfolds to its functional shape to permanently block the entrance to the LAA, thus preventing blood accumulation and stagnation. While easy to deploy, there are several risks associated with this device. It sometimes has difficulty conforming to the precise LAA opening. Nearly 15% of patients receiving these devices have experienced incomplete sealing of the LAA (and, thus, incomplete blockage of emboli), and they have required anti-coagulants after the procedure. The risks (aside from minimal risks of catheterization) include those of any implanted device. Up to 12% of patients had procedure-related adverse effects including device foreign body embolization, infection, perforations caused by the device, cardiac tamponade, and stroke [1e 1g].

Other physical plugs have also been utilized for occlusion purposes. The Amplatzer cardiac plug uses the same deployment mechanism as the Watchman plug for occluding the appendage. Additionally, like Watchman, it has difficulty conforming to the opening of the LAA, again allowing for potential emboli escape. Moreover, the same foreign body risks are applicable. As a result, it is not an ideal choice for treating AF-induced stroke potential.

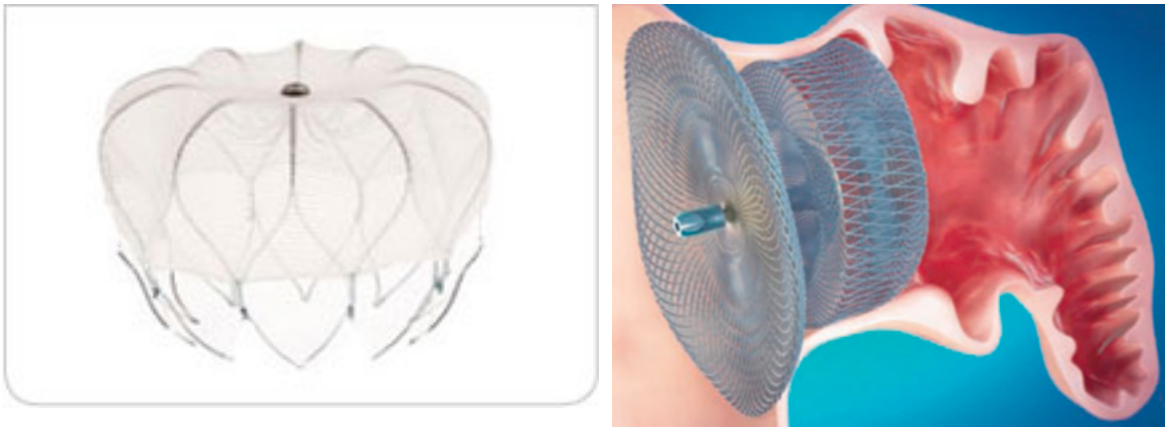

(a) (b)

Figure 1.4: LAA Occlusion Devices: (a) Watchman [1g] and (b) Amplatzer [1h]

Scope of Research

This dissertation focuses on designing a more safe and effective method for completely occluding the Left Atrial Appendage with fewer negative sequelae. It investigates the hypothesis that a flexible material will more effectively conform to the unique geometry of the LAA than the rigid ones that have been utilized. Research focuses on the design of a more flexible catheter-placed occlusion system and the confirmation of all the subfunctions that can be completed successfully.

There are multiple criteria that the filling material must satisfy. Due to its application deep in the body, the material must be biocompatible, and it must possess low toxicity. The material must also promote endothelial cell growth, as this tissue overgrowth is necessary for permanent occlusion. The material must not degrade before this tissue growth occurs either. Finally, the material must have favorable fluid properties so that it can be transported to the LAA through a

catheter. Ideally, viscosity of these hydrogel aqueous solutions would be low enough such that they can be delivered by hand power – a method highly preferred by surgeons.

Multiple hydrogels were considered as filling materials for this application. Fibrin-based hydrogels, while exhibiting a low degree of toxicity, can create clots, and, therefore, prove unsafe for this particular application. Calcium alginate was also considered, but it was deemed unsuitable due to its degradation time being too fast for tissue overgrowth. Finally, Polyethylene glycol-based photopolymers were also investigated. These hydrogels start as liquid aqueous solutions until exposed to Ultraviolet (UV) light, which initiate crosslinking and solidification. Use of these latter materials would add an additional complexity to the procedure of delivering UV light to the LAA; that is, solidification time would be increased, as well as would be overall procedure time -- both undesirable effects of using these polyethylene glycol-based photopolymers for this application.

Preliminary research has identified a hydrogel to be used in the occlusion, one that consists of a combination of PEG-tetra-thiol and Dextran vinyl sulfone (referred to as PEG and Dextran or DEX in the rest of this document). The material has a high degree of biocompatibility, and very low toxicity when introduced into the body. Additionally, PEG and Dextran components stay in liquid form when kept separate, but they begin solidifying almost instantaneously when the two components are combined. Research experimentally measured fluid properties of

the hydrogel's components, as well as the hydrogel's material properties, so as to evaluate its viability as a filling material for this application in occluding the LAA. [1i 1j].

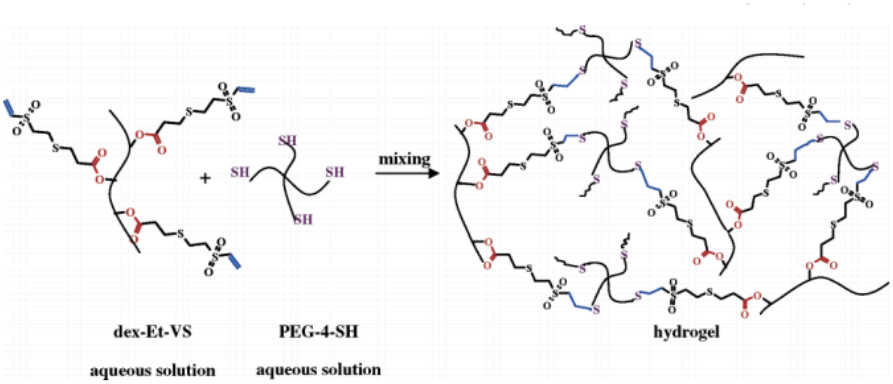

Figure 1.5: PEG and Dextran hydrogel components before and after crosslinking [1i].

Due to the fast solidification time of PEG and Dextran hydrogels, it proves very difficult to combine components outside the body. Under current implementation, the hydrogel material will be delivered through a femoral cardiac catheter. Once inserted in the leg, the catheter will travel up the femoral vein into the desired position in the heart (Figure 1.6). Aqueous PEG and Dextran solutions will be transported separately, and the two solutions will be mixed at the tip of the catheter right before entering the appendage and solidifying. This current research has investigated the optimal mixing chamber in which to combine these two components. Using experimentally determined viscosity and density measurements, laminar fluid flow was modeled in the separate mixing chamber designs. A prototype of the optimal mixing chamber was also fabricated to validate this experimental model.

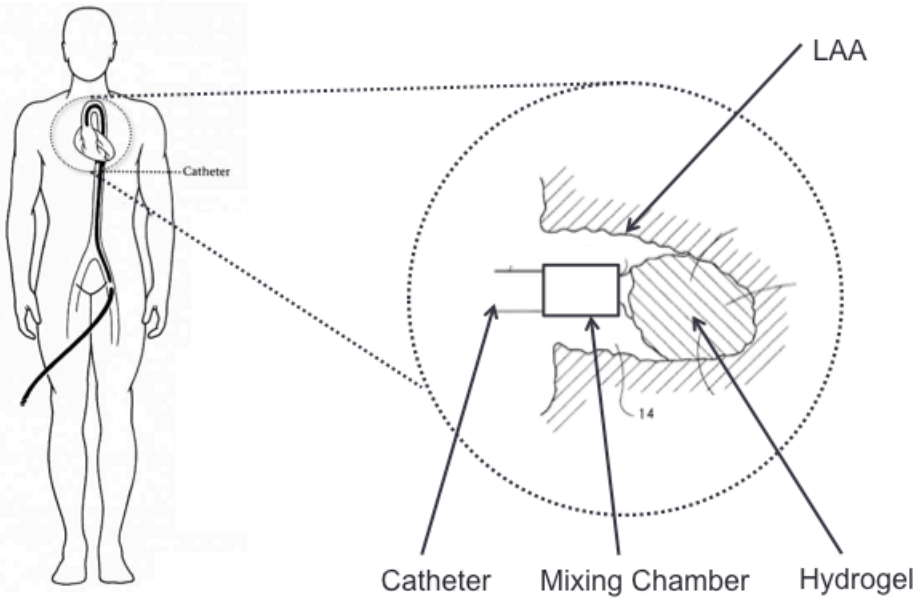

Figure 1.6: Conceptual in-situ delivery of hydrogel components [1k]

Chapter 2: Material Testing of Hydrogel Components

Previous work has identified a PEG-Dextran hydrogel as a potentially suitable filling material for the occlusion procedure. Its biocompatibility and solidification time indicate it can successfully occlude the LAA in a manner promoting endotheliazation and complete tissue overgrowth. However, it was unknown whether this material possessed favorable fluid transport and degradation properties for such an application. To better evaluate the suitability of the hydrogel for this application, multiple material properties were experimentally determined. Experimentation looked at density and viscosity, degradation rate, volumetric swelling ratio, and setting time for the hydrogel.

Within the candidate material, there are additional modifications that can affect material performance. These variations affect crosslinking ability and can cause changes in fluid and material properties. The first variation involves changing the concentrations of PEG and Dextran components in aqueous solutions. The second involves Direct Substitutions (DS) in Dextran side chains. These substitutions promote crosslinking, thereby leading to additional material swelling and strength. To better understand how these configurations affected hydrogel performance, part of this experimentation looked at correlations between concentration or DS number and the material properties. Correlations between these configurations and properties were measured, and examined for statistical

significance. For this work, 95% confidence interval was considered statistically significant.

Formation of Hydrogels

Controlled masses of PEG and Dextran were mixed with a controlled volume of TEA buffer. Samples were made with varying concentrations of hydrogel in the buffer, measured in terms of wt. %/vol. (g/cm^3). Samples ranging from 10% to 40% wt./vol. were examined in this study. Additionally, two different types of Dextran, with different DS numbers, were examined (DS 5 and DS 10). In this chapter, hydrogel samples are denoted by their concentration, as well as by the type of Dextran used. This preparation method was used to create the all samples used in testing described below.

Density and Viscosity Measurement

PEG and Dextran samples were prepared as described in the previous section. Next, controlled volumes of samples were taken and weighed. Knowing the mass and volume of each sample, density was calculated. Results are shown in Table 2.1 below. For all materials measured, there is a statistically significant correlation between concentration and density.

Table 2.1: Density of PEG and Dextran samples for varying samples and concentrations

Density (g/cm^3) of Materials					
	Concentration	**10%**	**20%**	**30%**	**40%**
Material	PEG	1.080	1.202	1.295	1.393
	Dextran DS 5	1.120	1.191	1.305	1.395
	Dextran DS 10	1.107	1.193	1.306	1.399

After taking these measurements, samples were heated to 37°C in a water bath. Kinematic viscosities were measured using size 75 and size 150 Canon Manning Semi-Micro glass capillary viscometers. Once kinematic viscosity in each sample was measured, dynamic viscosity of the sample was calculated using the following relation:

$$\upsilon = \frac{\mu}{\rho} \tag{2.1}$$

In this formula, υ represents kinematic viscosity; μ stands for dynamic viscosity; and ρ is the density of the measured material. For each sample, viscosity was measured 12 times to ensure accuracy. The mean values of these multiple trials, as well as standard deviations for each material and concentration, are shown in the tables below.

Table 2.2a and b: Kinematic (top) and Dynamic (bottom) Viscosities of Material for Varying Concentrations

Kinematic Viscosity (cStr)								
Concentration		10%		20%		30%		40%	
		Visc.	STD	Visc.	STD	Visc.	STD	Visc.	STD
Material	PEG	2.452	0.021	6.467	0.053	19.1	0.115	23.556	0.070
	Dextran DS 5	1.598	0.029	3.239	0.049	5.649	0.044	8.51	0.026
	Dextran DS 10	1.451	0.020	3.416	0.048	4.96	0.066	11.673	0.167

Dynamic Viscosity (cStr)								
Concentration		10%		20%		30%		40%	
		Visc.	STD	Visc.	STD	Visc.	STD	Visc.	STD
Material	PEG	2.646	0.023	7.773	0.064	24.729	0.149	32.81	0.097
	Dextran DS 5	1.789	0.032	3.859	0.058	7.371	0.057	11.871	0.036
	Dextran DS 10	1.607	0.022	4.075	0.056	6.478	0.086	16.335	0.233

As expected, an increase in concentration caused an increase in viscosity. The correlation between viscosity and concentration was statistically significant for both PEG and Dextran DS 5. The lack of significance for Dextran DS 10 was likely due to the low number of data points for each material, and taking measurements at more concentrations would likely confirm a correlation. In addition, standard deviations were relatively small relative to measured viscosity (<1.4% for all materials and concentrations). It would be beneficial, however, to determine if there is a known relationship between polymer concentration and viscosity. This would allow for prediction of viscosities of aqueous solutions at various concentrations. In the past, concentrated polymer suspensions have been defined with the Kreiger-Dougherty model [2a]. The equation for this model takes the following form:

$$\frac{\eta}{\eta_o} = (1 - \frac{\phi}{\phi_m})^{[\eta]\phi_m} \quad (2.2)$$

In this equation, η is the viscosity of the entire suspension; η_o is the viscosity of the solute (in this case, TEA buffer); ϕ is the volume fraction of the suspension; ϕ_m is the maximum volume fraction of the suspension; and [η] is the intrinsic viscosity of the polymer.

Volume fraction was calculated using the density of polymers (1.07 g/cm^3 for PEG, and 1.109 g/cm^3 for Dextran [2b 2c]). This value was used to calculate the volume of polymer, V_p, that was required to create the desired concentration for an aqueous solution of designated volume, V_a. Volume fraction was calculated with the following equation:

$$\phi = \frac{V_s}{(V_s + V_a)} \quad (2.3)$$

Max Volume Fraction, ϕ_m was calculated using the method above, for a 50% wt/vol. solution. The value of ϕ_m is .318 for PEG and .323 for Dextran.

Intrinsic viscosity is a measure of a polymers contribution to solution viscosity, and affected by molecular weight. A relation between molecular weight and intrinsic viscosity is described by the Mark-Houwink equation, which is presented as follows [2d]:

$$[\eta] = KM^a \quad (2.4)$$

Here M is the molecular weight of the polymer, and K and a are constants based on the particular material under investigation. There is some difficulty in finding precise Mark-Houwink parameters for the aqueous solutions of interest, despite previous research in this area. These parameters are affected by material type, as well as solvents used for the aqueous solution. There is also little data available for polymer solutions that use TEA buffer as a solute. Therefore, it is impossible to find exact parameters for materials. However, using a range of previously measured values for various types of PEG and Dextran (shown in Table 2.3 below), an intrinsic viscosity could be calculated -- one that leads to an accurate regression [2e-2g].

Table 2.3: Previously measured Mark-Houwink parameters for PEG and Dextran

Parameter	PEG	Dextran
K	.00075-.006	.005-.007
a	.7-.78	.7-.74

Table 2.4 below shows parameters selected for the KD regression, as well as R^2 value that result from the regression.

Table 2.4: Variables Krieger-Dougherty parameters as well as R^2 values from the resulting regression

Paramter	**PEG**	**Dextran**
K	.00485	.0062 (DS 5), .0068 (DS 10)
a	.77	.7 (DS 5, DS 10)
Φ_m	.318	.323 (DS 5, DS 10)
R^2	.69	.877 (DS 5), .978 (DS 10)

Plots of Krieger-Doherty projections vs. experimental data are shown below. While there is some variation in measured values (as noted in in table 2.2b), this variation is too small to be visualized on these plots. While increasing polymer

concentration increases solution viscosity, R^2 values are low for most materials, and it is currently unclear if our findings do, indeed, fit the Krieger-Doherty viscosity model. This is partially due to the lack of data points investigated for the current study. Future work could investigate additional concentrations to confirm if this model is accurate.

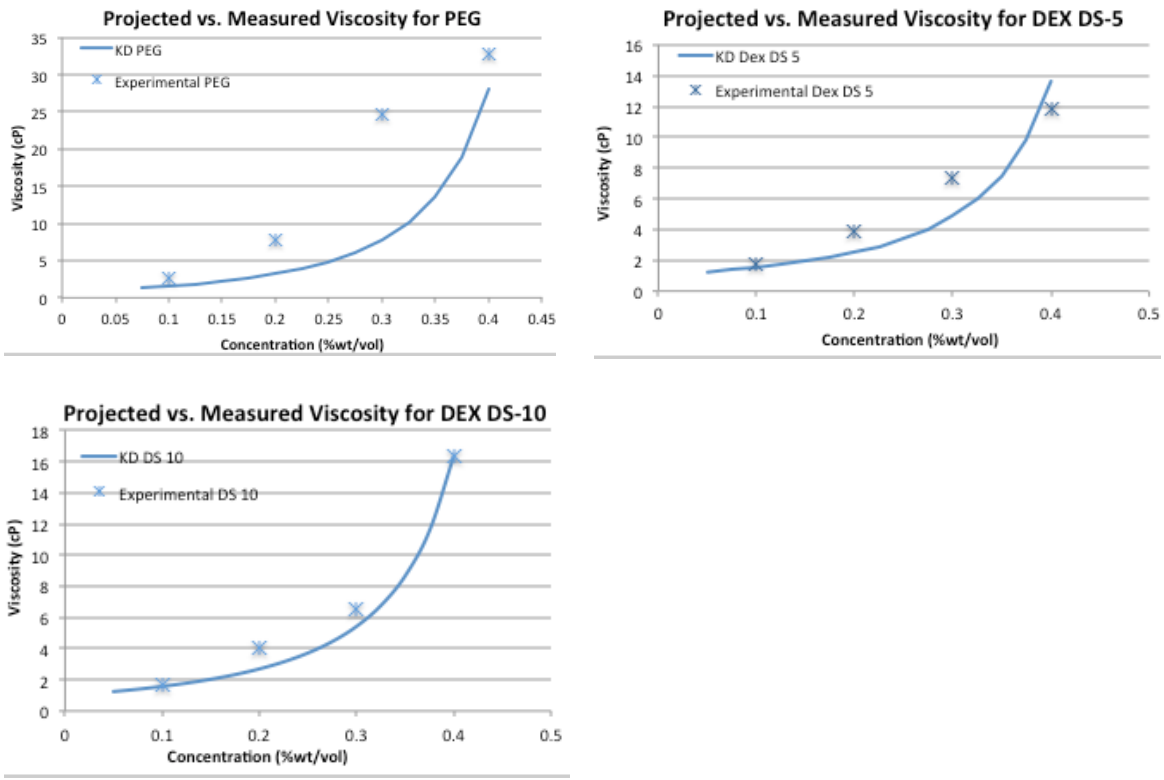

Figure 2.1: Experimental and Regression Plots for Aqueous Solution Viscosities

Degradation Trials

Samples of PEG and Dextran were mixed in a 1:1 ratio and allowed to solidify. In this study, 150 µL of each component was used. Samples were allowed to sit for two hours to allow complete solidification. To simulate human body

conditions, samples were then submerged in a .1% PBS buffer (PH 7.4), and rotated in a 37°C incubator. Samples were weighed at specified times to gauge what amount of the mixed material remained. For this study, degradation samples were measured in terms of equilibrium swelling ratio, which is defined as follows:

$$equilibrium\ swelling\ ratio\ Q_m = \frac{w_t}{w_o} \tag{2.5}$$

In this equation, w_t is the swollen weight and w_o is the unswollen weight of hydrogel. This dimensionless value allows for prediction for any size hydrogel sample.

Initially, the material solidified into one piece, and then swelled for about two days. Once maximum swelling was reached, samples would degrade slowly, throughout the bulk of the material. Samples were considered no longer usable for this application when they had broken into multiple pieces, or when visible pieces of hydrogel had broken off the main bulk. When degradation trials were stopped at 141 days, DS 10 30%, DS 5 40%, and DS 10 40% samples were viable, whereas the other samples were not. Results of these degradation trials are shown in Figures 2.2a and b below.

As expected, higher concentrations of material degrade more slowly. Additionally, higher rates of direct substitution in Dextran lead to slower degradation. This indicates that the hydrogel can be customized depending on the desired length of application needed. Additionally, all material degradation has an exponential decay, and it possible to extrapolate the material present at a given

time. This allows us to predict material degradation for long-term applications, as well as the anchoring force of the material within appendage.

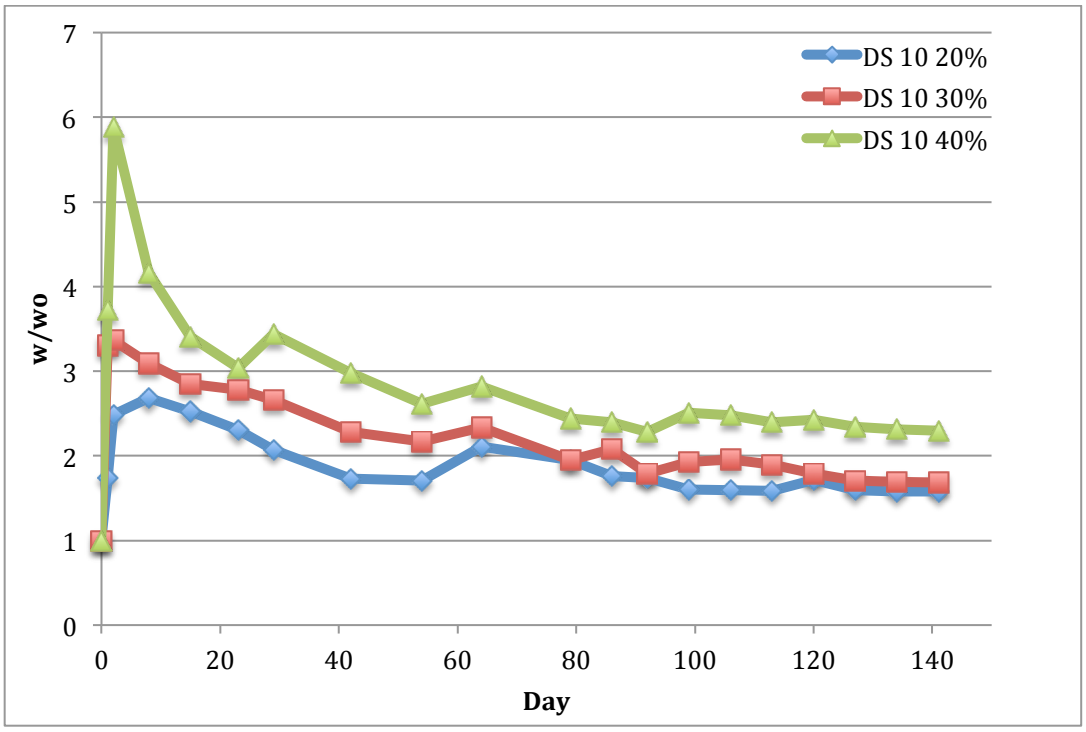

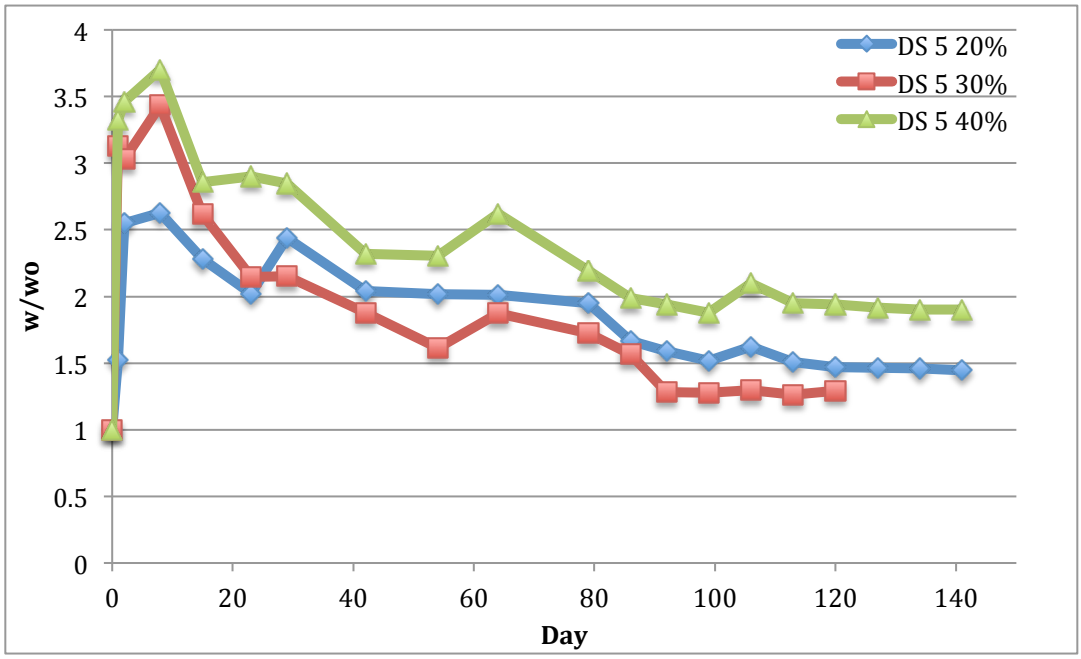

Figure 2.2a and b: Degradation Trial Data for DS 5 (top) and DS 10 (bottom) samples

One outlier to the trends listed above was the DS 5 30%/vol. sample. This sample degraded faster than all others, including the DS 5 20% hydrogel. This result was probably an anomaly, however, and this sample should degrade at a rate between that of DS5-20% and DS5-40% samples. For an unknown reason, this sample appeared to break up faster than other samples. Because this result was probably an anomaly, DS5-30% would likely have a degradation rate consistent with trends described above.

Solidification Time Measurement

It is important to be able to better quantify the solidification time of the hydrogel. Additionally, the catheter balloon cannot be deflated before material solidifies completely, or the still-liquid hydrogel would leave the LAA. This can lead to incomplete sealing, as well as other adverse effects that could be potentially fatal.

Samples of PEG and Dextran DS 5 were prepared as described above at varying concentrations. 50 uL samples of each component were combined in a vial and shaken vigorously until components were completely mixed. Solidification time was defined as the time from when components were initially combined to the time when material would no longer move within a tilted vial. For each concentration, 5 solidification trials were performed. The average time for each concentration are

shown in the Figure 2.3, with error bars designating one standard deviation for solidification time.

Table 2.5: Solidification Time of Hydrogel for Varying Concentrations

Concentration	Mean Solidification Time (s)	STD (s)
20%	99	2.94
30%	84	5.48
40%	58.25	2.22

Concentration of material is inversely proportional to solidification time, and there is a statistically significant correlation between concentration and solidification time. This is likely due to higher concentrations having a faster rate of crosslinking. Additionally, standard deviations for solidification time is relatively small (<6.6% of mean solidification time for all samples), indicating solidification times are relatively consistent. This indicated that a high degree of repeatability for all hydrogel solidification.

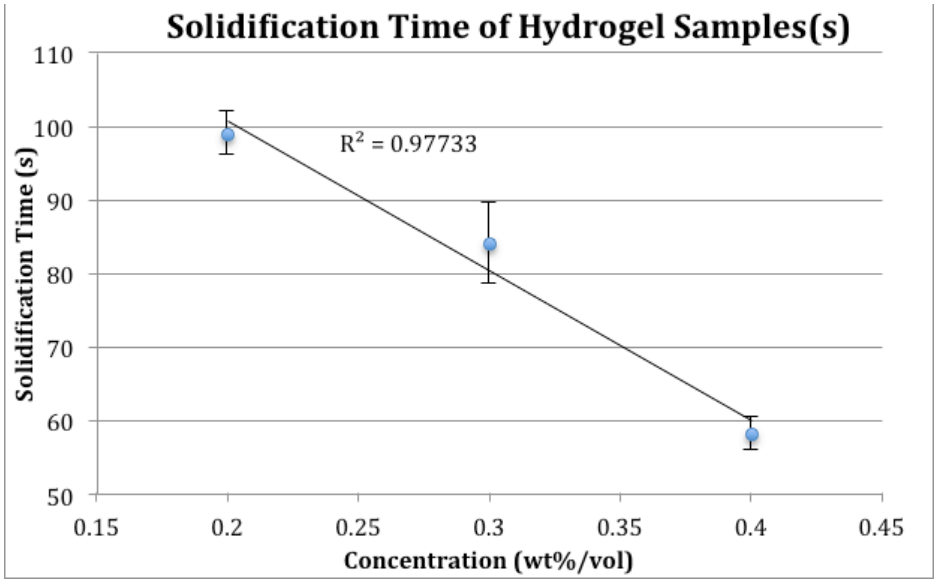

Figure 2.3 Plot of Solidification Time for DS 5 Hydrogels at Varying Concentrations

Due to low material availability, it is unclear how changing the DS number of Dextran would affect solidification time. It is believed that higher DS numbers would lead to a decrease in solidification time. However, future experimentation with additional material samples of varying DS number will be necessary to confirm this hypothesis.

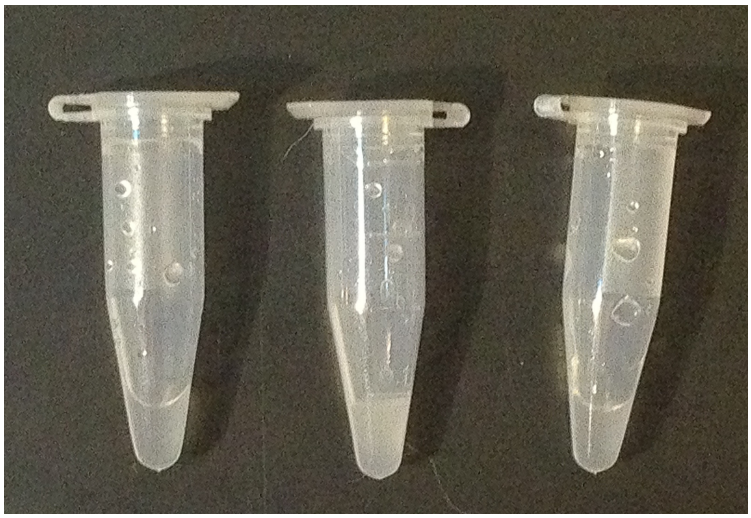

Figure 2.4: Hydrogel samples from solidification time trials

Volumetric Swelling Ratio

During degradation trials, all materials seemed to swell significantly. Maximum swelling was often observed after 1-2 days submerged in buffer. Higher concentrations and DS numbers also seemed to cause more swelling in terms of mass. To better understand the relationship between material configurations and volumetric swelling, testing was done to specifically quantify volumetric swelling.

Samples from the solidification trials described above were allowed to sit for 2 hours to solidify completely. For each aqueous solution concentration, 5 separate hydrogel samples were used. Samples were then submerged in PBS buffer, and allowed to swell. Every 24 hours, samples were removed from the buffer and dried, and the samples volume was measured, using a graduated cylinder. Volumetric swelling ratio is defined as:

$$volumetric\ swelling\ ratio = \frac{V_t}{V_o} \tag{2.6}$$

In equation 2.6, V_t is the swollen volume, and V_o is the unswollen volume of hydrogel. A plot of mean swelling ratios for various polymer concentrations is shown in the Figure 2.4 below.

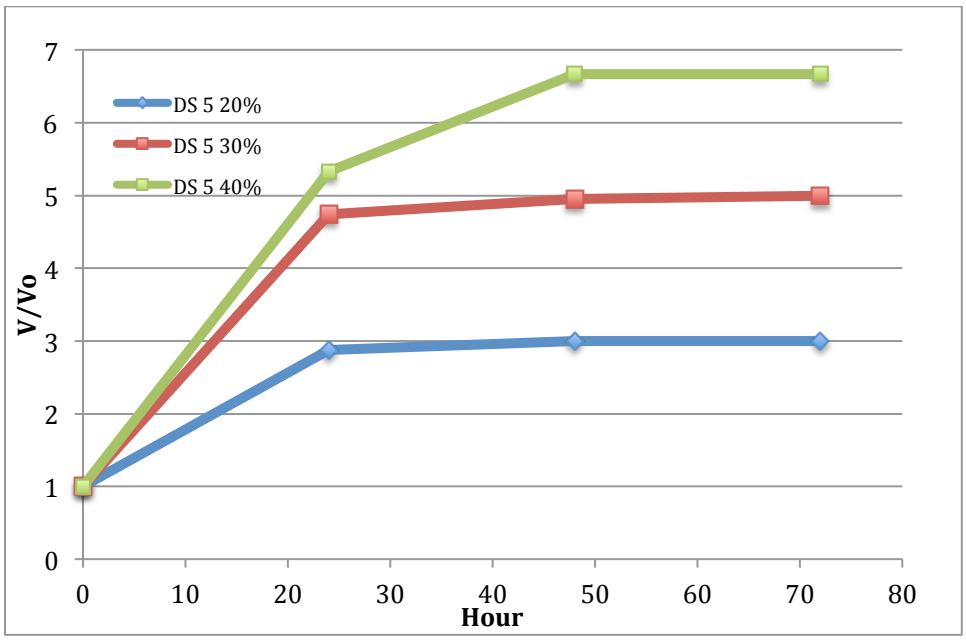

Figure 2.5: Volumetric Swelling Ratio for various hydrogel concentrations

Aqueous solutions with higher concentrations lead to higher volumetric swelling. This swelling is desirable, however, as it will increase anchoring force of

the hydrogel in the LAA. An additional observation from these trials is that most swelling for each sample configuration occurs within the first 24 hours. However, because measurements were only taken once per day, it is unclear how the material swells in between hours 0 and 24. It is of interest to know how the material swells during this time period, as it is an indicator of how anchoring force ramps up after the occlusion procedure. Future trials could measure volume of the samples over a more frequent time scale, to better understand this initial swelling.

Based on this material experimentation, this device should use an aqueous solution with higher hydrogel component concentration and DS number. DS 10 30% and DS 10 40% would be optimal choices. These samples exhibit both the best degradation and the best swelling characteristics. While these samples do have higher viscosities, the measured values are not too high to prevent transport through the catheter in the body. Chapter 3 will discuss analysis of transfer of material in more detail.

Hydrogel Anchoring Analysis

Once the hydrogel is transported and solidified in the chamber, it is important that it does not move or become dislodged from the chamber. To confirm that this would occur in actuality, an anchoring analysis was done. This analysis looked at swelling of the hydrogel and the resulting interface pressure. Next it examined anchoring force that results from this interface pressure.

Degradation trials data described previously in this chapter were done to analyze material composition over time. From these trials, it is possible to extrapolate a projected swelling ratio at 180 days (the time needed for complete endothelial tissue overgrowth). For this analysis, equilibrium swelling ratio (based on mass measurements) was used for the study. While volumetric swelling ratio would give a more accurate projection, long-term volumetric degradation data was not available for analysis. As a result, it was assumed that volumetric degradation was approximately proportional to mass-based degradation.

For this model, it was assumed that the material undergoes isotropic swelling, and that the swelling in terms of mass corresponded to a dimensionally similar volumetric swelling. Change in hydrogel plug radius can be predicted based on these swelling ratios with the following relationship:

$$Radius\ Multiple, R_m = \frac{R_{swollen}}{R_{initial}} = {Q_m}^{1/3} \qquad (2.7)$$

The tables below show projected Q_m and R_m at 180 days.

Table 2.6a and b: Projected swelling ratio (left) and material radius (right) at 180 days

Material Sample	w/w_o at Day 180
DS 5 20%	1.449
DS 5 30%	1.117
DS 5 40%	1.767
DS 10 20%	1.509
DS 10 30%	1.686
DS 10 40%	2.165

Material Sample	R/R_m at Day 180
DS 5 20%	1.131
DS 5 30%	1.037
DS 5 40%	1.208
DS 10 20%	1.146
DS 10 30%	1.190
DS 10 40%	1.293

To analyze anchoring force, the interface pressure between the expanding materials was calculated. The interface pressure between the hydrogel plug and LAA tissue is defined with the following equation:

$$\text{Interface Pressure}, p_i = \frac{\delta_r}{\frac{R}{E_o}\left(\frac{r_o^2 + R^2}{r_o^2 - R^2} + \nu_o\right) + \frac{R}{E_i}(1 - \nu_i)} \; [2h] \tag{2.8}$$

In this equation, δ_r is the change in hydrogel radius due to swelling; R is the initial radius of the hydrogel plug; r_o is the OD of LAA tissue; and ν_o and ν_i are Poisson's ratio for tissue and the hydrogel, respectively. E_o and E_1 are the elastic modulus of the tissue and hydrogel, respectively. Values used in this analysis are shown in Table 2.7 below [2i 2j]:

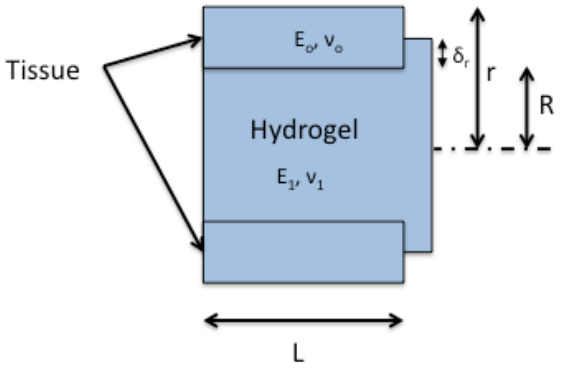

Figure 2.6: Dimensions used for anchoring analysis

The anchoring force of the hydrogel is defined as:

$$F = \pi d L_h p_i \mu_f \tag{2.9}$$

Here, p_i is the interface pressure described previously; d is the diameter of the hydrogel (equal to 2R); L_h is the length of contact surface between tissue and hydrogel; and μ_f is the coefficient of friction between LAA tissue and the hydrogel.

Values for this analysis were based on previously measured values from literature [2k].

Table 2.7 Values Used in Anchoring Analysis

Variable	Description	Value
δ_r	Change in hydrogel radius	Varies by sample
R	Initial radius of hydrogel	10 mm
r	Initial radius of hydrogel and tissue	11 mm
E_o	Elastic modulus of tissue	40.8 kPa
E_1	Elastic modulus of hydrogel	14 kPa
ν_o	Poisson Ratio of tissue	.45
ν_1	Poisson Ratio of hydrogel	.5
d	Diameter of hydrogel	20 mm
L_h	Length of hydrogel	30 mm
μ_f	Coefficient of friction	.332

For a material to be acceptable for this application, the minimum anchoring force would have to be large enough to support the weight of the plug. Experimentally measured values for density were used to determine the weight of a hydrogel plug. The table below shows the weight of a plug for each sample, as well as the projected anchoring force for each, based upon projected swelling ratios at day 180 and the equations above.

Table 2.8: Projected weight and anchoring force of plug for various hydrogel concentrations

Sample	Density (g/cm3)	Weight of plug (N)	Projected Anchoring Force (N)	Anchoring Force/Plug Weight
DS 5 20%	1.195	.221	.277	1.253
DS 5 30%	1.300	.240	.078	.325
DS 5 40%	1.395	.258	.444	1.721
DS 10 20%	1.195	.221	.310	1.403
DS 10 30%	1.300	.240	.403	1.679
DS 10 40%	1.395	.258	.631	2.445

Based on the results above, all samples other than the DS 5 30%, will create sufficient anchoring forces, and have a safety factor of 1.25 or higher. The low value for the DS 5 30% sample was likely due to anomalous degradation data. A more reasonable range for anchoring force would be .277-.444N (in between DS 5 20% and DS 5 40% samples). All values for this range provide sufficient anchoring forces, and it is believed that this anomalous sample would provide sufficient anchoring as well.

It is worth noting that this analysis represents the most conservative anchoring scenario. Additional anchoring forces due to blood pressure and geometric anomalies like irregular trabeculae or multiple lobes in the LAA were not considered [2l]. Blood pressure would likely only act on the outer surface of the hydrogel (the surface facing the LA), providing additional anchoring force. Irregular trabeculae and geometric asymmetries in the LAA would also cause additional anchoring, but these were not quantified due to unpredictable geometry in the LAA. Both of these would add additional anchoring, and provide further evidence that this hydrogel is suitable for application in occluding the LAA.

Conclusion

The candidate filling material was tested in multiple configurations for its ability to occlude the appendage. Experimentation analyzed fluid properties of uncured hydrogel components. These properties were later used to examine

transport of these components through the catheter (this work is described in the next chapter). Additional investigation looked in to material properties like swelling ratio and solidification time. These tests confirmed that the material behaves in a way that is favorable to the desired application.

Chapter 3: Fluid Transport Analysis

The device must be readily able to transport fluids in and out of the catheter to the LAA. While multiple pressure sources are plausible, all power in this design would most likely come from a surgeon's hand during the procedure. This power source would allow a surgeon a high degree of control during the occlusion procedure, and therefore, is the preferred delivery mechanism for the invention.

Design Parameters

Three independent fluids are transported during the occlusion process and were taken into consideration during this analysis. Once the LAA is isolated, any fluid in the chamber will be removed by suction pressure from a syringe. While the LAA will primarily contain blood, this blood might be mixed with a contrast agent for imaging or with saline to promote fluid flow. Three separate fluids were analyzed for drainage: pure blood; a 50%-50% by volume combination of blood and contrast agent; and 50%-50% by volume combination of blood and saline – were analyzed for drainage. Once the LAA is fully drained in the procedure, hydrogel components are pumped into the chamber simultaneously at equal flow rates in separate lumens. Hand force must provide sufficient driving pressure for both these transport steps.

Previous experimentation has found that the index and middle fingers can provide an average of 105 N of pinch force [3a]. This represents an upward limit to the amount of force a surgeon's hand can provide to a syringe during the occlusion

procedure. Fluid in the LAA will likely be removed with a single 30cc syringe, which typically has an ID of .891 inches, or .0226 meters. Each hydrogel component will be transported simultaneously by a 20cc syringe, which typically has an ID of .776 inches, or .0197 meters [3b]. The following equation was used for determining syringe pressure, P_s:

$$P_s = \frac{F}{A} \tag{3.1}$$

Maximum pressure from hand force is 261.0 kPa during the drainage step, and it is 172.1 kPa during hydrogel transport. Driving pressure for all fluid transport must be less than these values in order to satisfy the design requirement that all fluid be transported by hand power.

One design requirement of the invention is that all fluids be transported in and out of the chamber in a single, multi-lumen catheter. Additionally, to allow for ease of insertion and positioning, this catheter must have a maximum diameter of 9 French (3mm), with all lumens fitting within this dimension. Under its current embodiment, the catheter will have 4 lumens: 2 for PEG and Dextran filling component transport; one for blood removal and guide wire navigation; and one for inflating and deflating the isolation balloon. The PEG and Dextran filling component transport lumens must be the same size in order to keep flow rates equal. The blood drainage lumen must be .95 mm in order to accommodate typical guide wires for

positioning the catheter. A cross section of this current embodiment is shown in Figure 3.1.

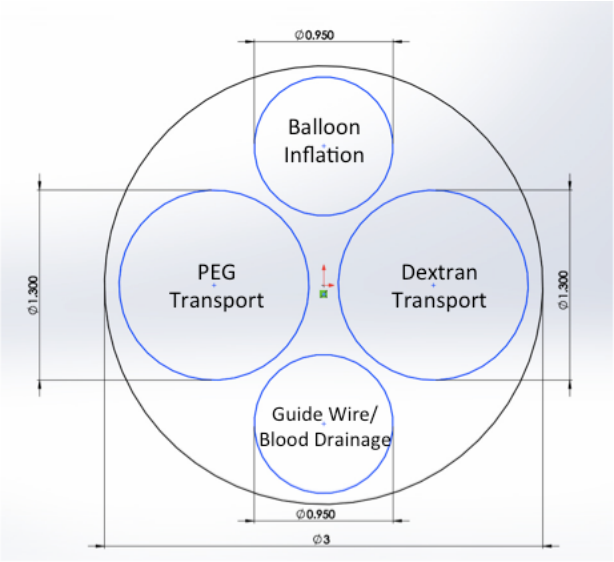

Figure 3.1: Cross section design for multilumen catheter

Governing Equations

All three fluids to be transported exhibit non-Newtonian behavior. A power law relation would typically be used to model the variation in viscosity. However, previous work has shown that, at high shear rates (>100 s^{-1} for blood and >250 s^{-1} for hydrogel components), these fluids exhibit Newtonian behavior. Due to the small lumen diameters within the catheter, fluids are predicted to always have high shear rates (>400 s^{-1} for all fluids) when transported. As a result, during analysis, it was assumed that blood and hydrogel components had a constant viscosity, and were modeled as Newtonian fluids. Viscosity values were taken from Merrill [3c], or experimentally measured, as described in Chapter 2.

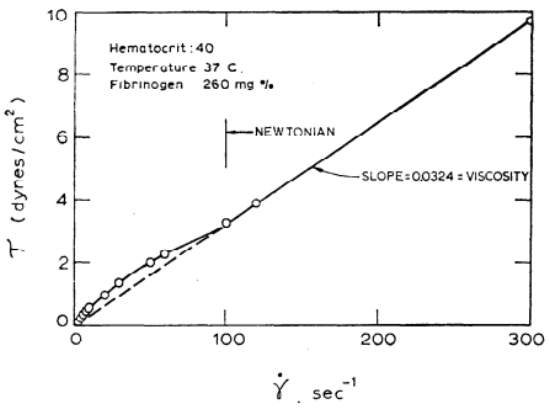

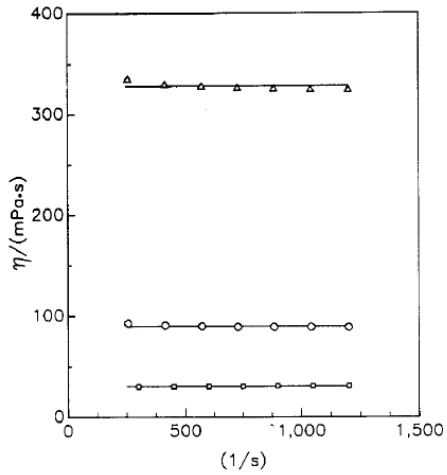

Figure 1. Influence of shear rates on the viscosity, η, for w(PEG)=0.40 at 277 K: (Δ) PEG 8000; (○) PEG 3350; (□) PEG 1000.

(a) (b)

Figure 3.2: (a) Shear stress vs. Shear rate for blood [3c] (b) Viscosity vs. Shear rate for PEG [3d]

To calculate driving pressure for a blood-saline or blood-contrast solution, it is important to first know the viscosity of the mixed solution. To find the viscosity of two mixed liquids, the Refutas Equation can be used [3e]. This equation is calculated in 3 parts. First, the viscosity blend number (VBN) is calculated for each fluid with the following equation:

$$VBN = 14.534 * \ln[\ln(\nu + .8)] + 10.975 \quad (3.2)$$

In this equation, ν represents the kinematic viscosity of the liquid in cStr. Values for kinematic viscosity were determined from the literature or measured experimentally. Values used in this analysis were 30.6 cStr for blood; 13.9 for contrast; and .994 for saline.

Once VBN numbers were calculated for each fluid, the overall number, VBN_{Blend}, was calculated for the mixture, using the following relation:

$$VBN_{Blend} = \omega_A * VBN_A + \omega_B * VBN_B + \cdots . + \omega_N * VBN_N \quad (3.3)$$

Here, ω_N is the mass fraction of the Nth liquid. Once the overall VBN number is calculated, kinematic viscosity of the liquid combination can be determined with the following equation:

$$\nu = \exp\left(\exp\left(\frac{VBN_{Blend} - 10.975}{14.534}\right)\right) - 0.8 \quad (3.4)$$

Values for kinematic viscosity were determined to be 19.6 cStr for a blood-contrast mixture and 7.20 cStr for a blood-saline mixture. This corresponds to a dynamic viscosity of 7.5 cP for blood-saline and 23.7 cP for blood-contrast.

For fully developed, internal, laminar flow, flow rate, Q, is defined as:

$$Q = \frac{\pi R^4}{8\mu}\frac{\partial p}{\partial x} = \frac{\pi \Delta p D^4}{128 \mu L} \quad (3.5)$$

In the equation above, Δp is the required driving pressure, R and D are the diameter and radius of the catheter lumen, respectively, μ is the dynamic viscosity of the fluid being transported, and L is the length of the channel. This equation can be rearranged to give the following relation for driving pressure based on a known flow rate [3f]:

$$\Delta p = \frac{128\mu LQ}{\pi D^4} \tag{3.6}$$

Minor losses due to bends and change in direction of the catheter, primarily occurring between the femoral vein and the heart, will lead to some additional pressure drop. Loss coefficients for these bends are based on the ratio between radius of curvature of the bend and diameter of the channel (r/D – see figure below). For the envisioned catheter embodiment, this ratio will be ~100. Any loss coefficient is inversely proportional to this ratio and approaches 0 for ratios of this magnitude. Additionally, this bend loss decreases if there is no change in height in the plane of the curvature (a situation that would occur when a patient is lying flat) [3g]. As a result, minor losses are small enough to be negated and are not considered in this analysis.

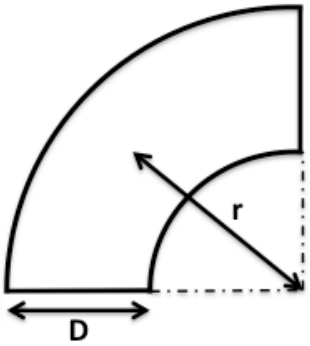

Figure 3.3: Radius of curvature, r, and channel diameter, D, used in determining minor loss coefficient.

Variables Used For Analysis

For patients with AF, the mean volume of the LAA is 22.9 mL [3h]. A flow rate of ~65 μL/s for each hydrogel component is required to fill the chamber in 180

seconds. (This time was a design constraint set for this analysis). A flow rate of ~127 μL/s is required to drain fluid in the chamber in the same amount of time. The catheter will have a length of 80 cm with an additional 5cm of length for each lumen to include the manifold and connectors for each channel. Table 3.1 below lists additional values used in this fluid analysis.

Table 3.1 Variables used for driving pressure calculations.

Term	Symbol	Value	Units
Volume of LAA	V	22.9	mL
Hydrogel Filling Time	t_h	180	S
Blood Drainage Time	t_b	180	S
Hydrogel Flow Rate	Q_h	65	μL/s
Blood Flow Rate	Q_b	127	μL/s
Hydrogel Lumen Diameter	D_h	1.3	Mm
Blood Lumen Diameter	D_b	.95	Mm
Catheter Length	L	80	Cm
Effective Viscosity of PEG	μ_{PEG}	32.8	cP
Effective Viscosity of Dextran	μ_{DEX}	16.3	cP
Effective Viscosity of Blood	μ_B	32.4	cP
Effective Viscosity of Blood-saline mixture	μ_{BS}	7.5	cP
Effective Viscosity of Blood-contrast mixture	μ_{BC}	23.7	cP

Results

When the variables from table 3.1 are plugged into the equations above, the driving pressure required for the hydrogel components is 25.3 kPa for PEG, and 12.6 kPa for Dextran. Driving pressure for removal of Blood, Blood-contrast, and Blood-saline solutions are 174.9 kPa, 128.0 kPa, and 40.5 kPa respectively.

Pressure drop from the mixing chamber must also be taken into account for this analysis. This pressure must be supplied in addition to the driving pressure for

hydrogel components through the catheter. Table 3.2 below shows pressure drop for different chamber designs given by COMSOL (this analysis is described in more detail in Chapter 5). Other modeling work showed the Serpentine chamber to have the most effective mixing, and the pressure drop in this chamber was used in further transport analysis.

Table 3.2 Pressure Drop for Mixing Chamber Designs

Mixing Chamber	Pressure Drop (Pa)
Microgroove	1417
Geometric Barriers	2527
Serpentine	1817

The table below shows overall driving pressure required for both blood removal and hydrogel transport steps. In all cases, hand force is sufficient to drive all fluid transport. This confirms our original hypothesis, as well as supporting hand force as the most desirable mode of delivery for maintaining surgical control of the procedure.

Table 3.3: Overall Driving Pressure for Fluid Transport

Procedure Step	Pressure (kPa)
Max Pressure from Hand Force	261 (blood), 172.1 (hydrogel)
Total Hydrogel Driving Pressure	40.4
Blood Removal Pressure	174.9
Blood-Saline Solution Removal Pressure	40.5
Blood-Contrast Solution Removal Pressure	128.0

Conclusion

This chapter examined the ability of a hand-powered syringe to transport fluid components through a catheter. This analysis used experimentally measured values from Chapter 2, previously measured fluid propertied from literature, as well as design parameters for the system. This analysis confirmed that hand power is a viable power source for transporting fluids into and out of the LAA.

Chapter 4: Balloon Isolation Modeling

Once the catheter is positioned in the body, a balloon is inflated at the opening of the chamber. This balloon will isolate the appendage during the occlusion procedure. Isolation will cover two functions. Initially, it will keep blood and other fluid in the LA and out of the appendage. In addition, it must also keep all hydrogel from leaking out of the LAA before it solidifies. To ensure a balloon can complete both of those tasks, potential designs were modeled in COMSOL to test their effectiveness.

Geometric Parameters

Two separate balloon geometries were considered for this study. The first is a long cylindrical balloon, with a radius of 10mm and a length of 15mm. Semi-spheres are attached to the ends, as is typical of surgical balloons. The second design considered has a tapered feature, with a slope of 5 degrees relative to the catheter. The larger end has a radius of 10mm, and the small end a radius of 8.7 mm. Like the cylindrical balloon, the balloon has a distal length of 15 mm, and semi-spherical caps at each end. Each balloon had a thickness of .2 mm (a typical thickness for angioplasty balloons [4a]). Each design is shown in Figure 4.1 below.

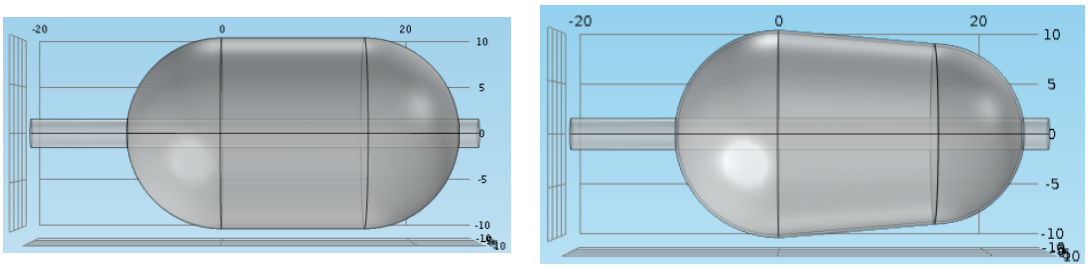

(a) (b)

Figure 4.1: Cylindrical (a) and tapered (b) balloon designs used in this model

The model also takes into account the opening of the LAA as well as the walls of the Left Atrium that are in contact with the isolation balloon. LAA opening geometry varies from patient to patient, and the balloon used must be able to work with all occurring appendage structures. To account for this variation in geometry, two different opening designs were used. The first is a circular opening with a radius of 10 mm. The second geometry used is elliptical, and it represents a more likely LAA shape. Diameters for this elliptical opening were 14.1 and 20.0 mm, which represent mean dimensions from previous investigations [4b]. These two opening geometries are shown in Figure 4.2 below.

Polyurethane was chosen as the material for constructing both the balloon and catheter for our model. This material has been used extensively for both multilumen tubing, as well as for catheter balloons used for angiograms and stent deployment, making it a suitable choice for this application. Previously measured material properties for polyurethane were used in construction of this model.

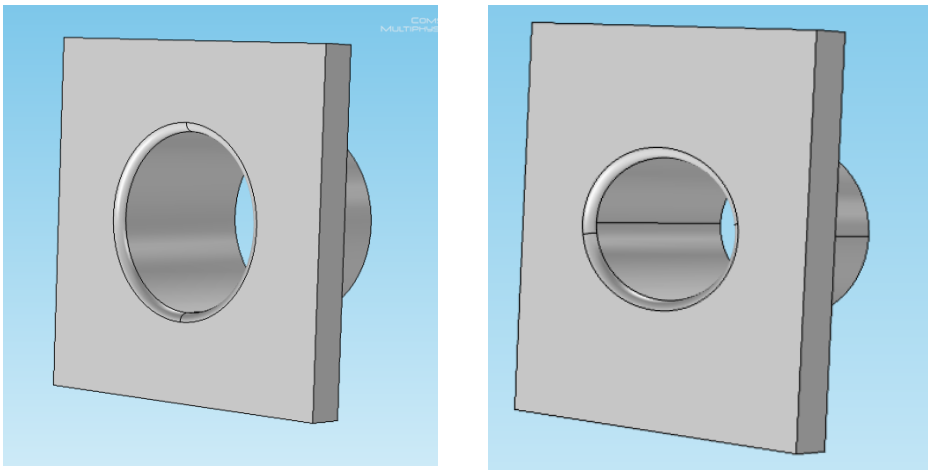

(a) (b)

Figure 4.2: LAA openings used in this model

A mesh for this model was automatically generated by COMSOL in a configuration that was optimized for Solid Mechanics. For both the balloon and tissue, each node had a maximum feature size of 1.4 mm. The circular and tapered balloons had 12281 and 13423 nodes, respectively. For appendage chamber openings, the circular opening chamber had 8100, while the elliptical opening had 9238 nodes.

Balloon pressure And Expansion

The balloon is inflated by filling with a pressurized liquid, typically transported through the catheter via an indeflator. This device, a syringe with threads on the shaft, allows for precise amounts of fluid transport, as well as for the ability to create consistent, precise pressure within the balloon. The liquid used for

inflation is usually a combination of saline and an iodine contrast agent for imaging. An indeflator like one that could be used in the device is shown in Figure 4.3 Below.

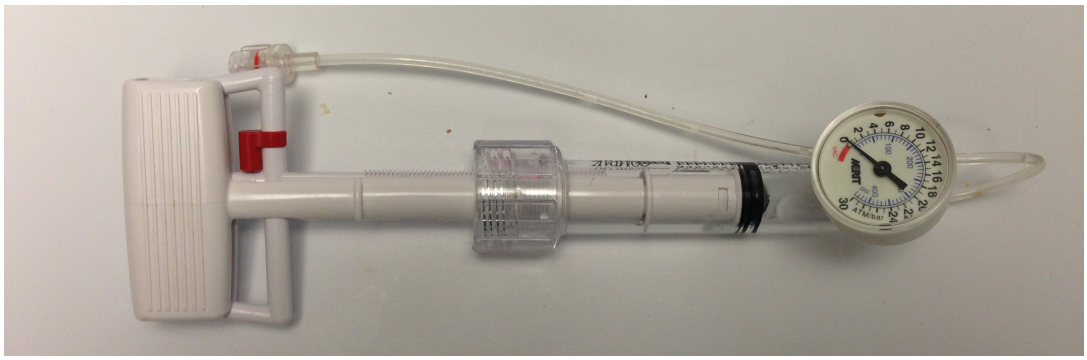

Figure 4.3: Medtronic Indeflator, with pressure gauge dial

For this model, a constant pressure, p_b, of 658.6 kPa (6.5 atm) was applied to the inside surface of the balloon. This corresponds to the lower spectrum of values typically used in balloon catheter procedures. While most catheter balloons are rated for higher pressured (as high as 20 atm in some cases), these pressures are typically encountered during stent deployment and angioplasty procedures. For our procedure, there is no need to deform tissue or any other material, and a lower pressure is acceptable in this embodiment. Additionally, to take blood pressure into account, a pressure of 3.3 kPa (25 mmHg), p_{LA}, was allied to the outer surface of the balloon. This is an upward limit for blood pressure found in the Left Atrium, and is applied to the outer surface of the balloon [4c]. Figure 4.4 shows pressures acting on the balloon.

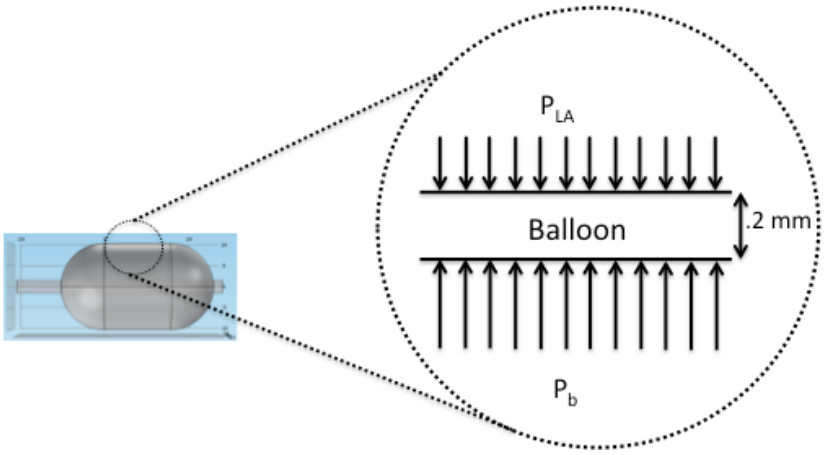

Figure 4.4: Diagram of pressures acting on balloon surfaces

Polyurethane has previously been shown to act as a hyperelastic material. Previously, Mooney-Rivlin models have accurately been used to model these materials for strain rates less than 2, and past work has used this model to examine balloon expansion during stent deployment [4d 4e]. This model, based on the generalized Rivlin model, has the following strain energy density function [4f]:

$$W = C_{10}(\bar{I}_1 - 3) + C_{01}(\bar{I}_2 - 3) \tag{4.1}$$

In the equation above, C_{10} and C_{01} are empirically determined material constants, which must be determined by measuring stress and strain, and taking a regression of this data [4f]. Determining the coefficients for this model would involve fabricating a balloon prototype, and testing it under controlled loading. This experimentation was considered too costly and time consuming for this model, and therefore unfeasible for this research. As a result, it was necessary to look for a different approach for modeling balloon expansion.

Another option for modeling balloon expansion is modeling polyurethane as a Linear-Elastic material. For small strain rates (~<.2 – See Figure 4.5 below), the relationship between stress and strain can be approximated as linear. In this model, polyurethane had an elastic modulus of 920 MPA, a density of 1070 kg/m^3, and a Poisson ratio of .495. One factor that must be taken into account is ensuring strain does not exceed the linear region. To ensure this model is accurate, strain must be calculated for each model, and confirm is does not exceed .2 in any area.

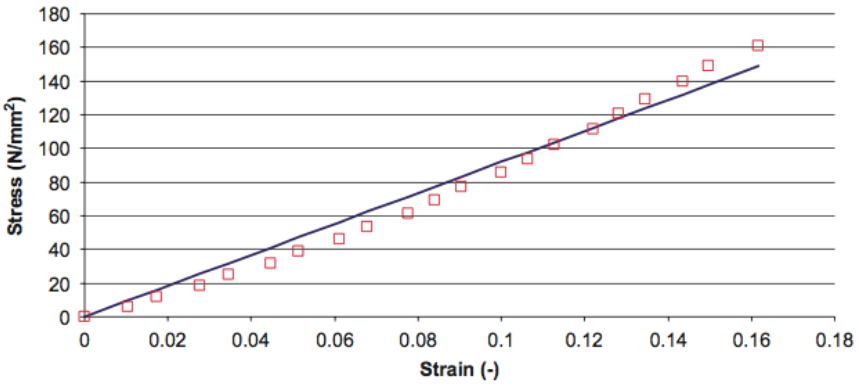

Figure 4.5: Experimental data and Linear Approximation for stress-strain relationship [4a]

For this model, cardiac tissue was also modeled as a Linear Elastic material. Previous work has modeled tissue in this way, and experimentation has looked at material properties for cardiac tissue. For the model, density of tissue was set at 1200 kg/m^3, Elastic Modulus E was set at 40.8 kPa, and Poisson Ratio set at .499 [4g, 4d].

Table 4.1: Material properties used in model

Variable	Description	Value
E_P	Elastic Modulus of Polyurethane	920 MPa
ν_P	Poisson Ratio of Polyurethane	.495
ρ_P	Density of Polyurethane	1070 kg/m^3
E_t	Elastic Modulus of LAA tissue	40.8 kPa
ν_t	Poisson Ratio of Tissue	.499
ρ_t	Density of Tissue	1200 kg/m^3

When positioning the catheter and moving it to the entrance of the LAA, the balloon must be compact for ease of transport. In the past, these balloons have been tightly folded around the catheter during transport (Figure 4.6), which then unfolds to its full size when inflated. For applications like stent deployment, or angioplasty, it is important that the balloon is inflated in a uniform fashion, so that no undesired distortions occur. For this application, however, we are only interested in the final, fully inflated state of a balloon. As a result, to lower the computational cost of this model, the balloon started in a semi-unfolded state, close to the balloon being fully inflated. At this point however, no part of the balloon is in contact with the tissue wall.

Figure 4.6: Balloon folded around catheter

Results and Analysis

Balloon designs were evaluated on their ability to completely isolate the chamber. Once models were computed, balloons and tissue were examined to confirm there was a full seal around the circumference of the opening. Additionally, to quantify sealing quality, analysis examined pressure exerted on the tissue by the balloon (as shown in Figure 4.7 below). It was important that the balloon was exerting force normal to the tissue surface around the entire circumference of the opening to ensure that no leakage would occur. Additionally, anchoring force is related to this interface interaction, and a larger total force will decrease the chance of the balloon shifting or dislodging during the procedure.

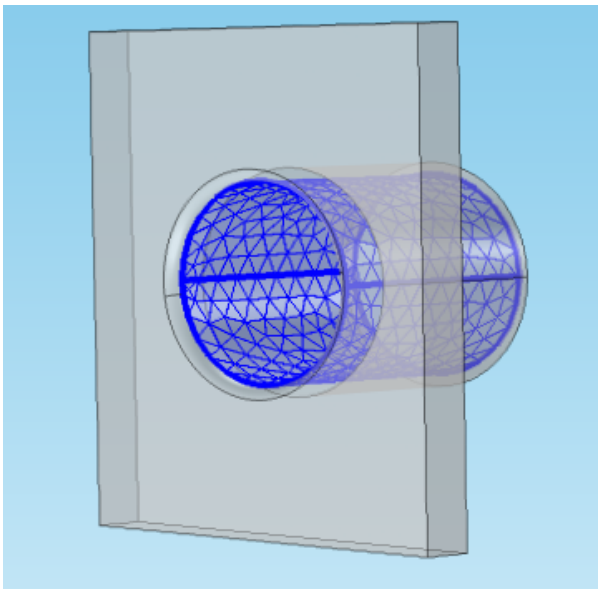

Figure 4.7: Tissue surface analyzed for quantification

Data for each node on the tissue surface in contact with the balloon was exported to MATLAB, and analyzed further. For each chamber and balloon setup, Average Interface Pressure and Total Interface Force were calculated. Average Interface Pressure was defined as:

$$\overline{P_i} \approx \frac{1}{N}\sum_{i=1}^{N} P \tag{4.2}$$

In the above equation, P is the normal force from the balloon at the i^{th} location, and N it the total number of data points. Total Interface Force was defined as:

$$F_i \approx \sum_{i=1}^{N} P\frac{A}{N} \tag{4.3}$$

Here, P is the normal force from the balloon at the i^{th} location, N it the total number of data points, and A is the surface area of the entire tissue surface.

Circular Chamber Opening

Both balloon geometries were able to completely seal the circular opening chamber, and balloon-tissue contact was established throughout the entire circumference of the chamber opening. This indicates that sealing of the appendage is possible for circular openings.

When analyzing the balloon deformation, there appears to be consistent, uniform pressure on the chamber walls. For the cylindrical balloon, this pressure is mostly consistent until the balloon starts to taper off at the end. For the tapered balloon, this pressure tapers off slowly, right up until the rounded edges of the

balloon, at which point pressure drops off more quickly. Surface plots of pressure of the balloon on tissue are shown in Figure 4.7 below.

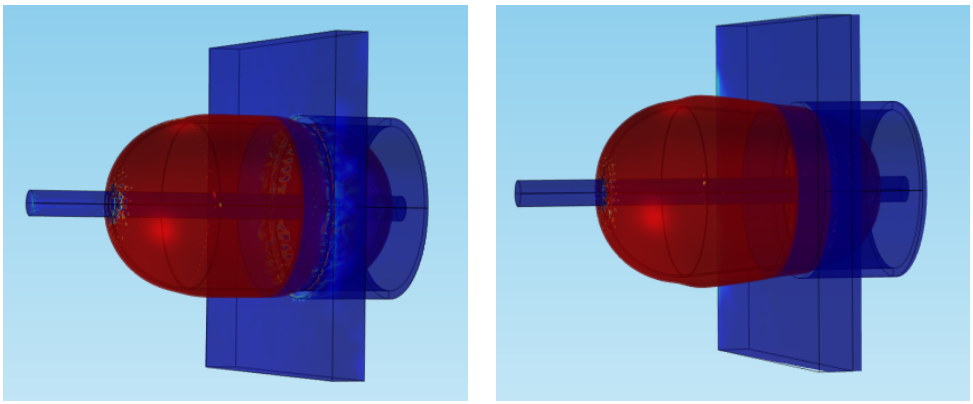

(a) (b)

Figure 4.8: Balloons sealing for (a) cylindrical and (b) tapered balloon

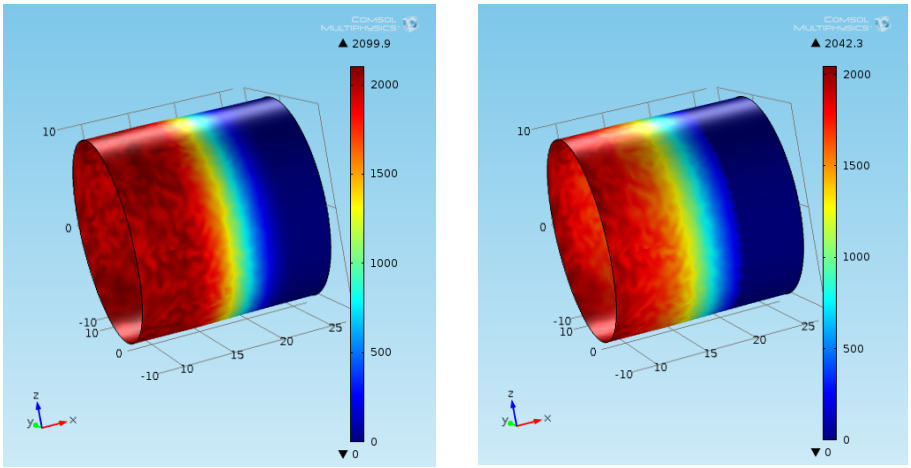

(a) (b)

Figure 4.9: Interface pressure for (a) cylindrical and (b) tapered balloon

When analyzing surface tissue data, the cylindrical balloon has an average interface pressure of 932 Pa, and a total interface force of 1.11N. The tapered balloon has an average interface pressure of 753 Pa, and a total interface force of .899 N. While both balloons showed complete sealing in this model, the cylindrical

balloon appears to produce a better seal, due to its higher average pressure and total interface force. Additionally, the number of individual nodes with surface pressure >0 was larger for the cylindrical balloon (288 vs. 219 for the tapered balloon). This indicated that the cylindrical balloon has a larger contact surface, further indicating that this balloon provided better sealing.

The model also looked at principal strains in all directions. Maximum principal strain at any point on the balloon was .0393 for both models. These values are all well below .2, confirming that the linear elastic model for the balloon is accurate.

Elliptical Chamber Opening

Once again, both balloons were able to form a complete seal around the circumference of the elliptical chamber opening. However, unlike the circular opening, pressure is not uniform around the chamber's circumference, and decreases for the longer radius of the opening. Like with the circular chamber opening models, the tapered balloon appears to have less balloon surface area in contact with heart tissue when expanded. From these observations, the cylindrical balloon appears to be a generally better choice for this application. Results from these models can be seen in Figures 4.9 and 4.10 below.

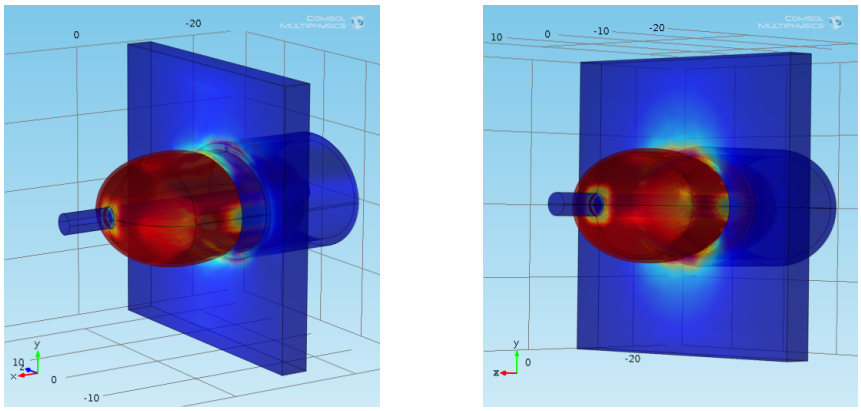

(a) (b)

Figure 4.10: Balloons sealing for (a) cylindrical and (b) tapered balloon

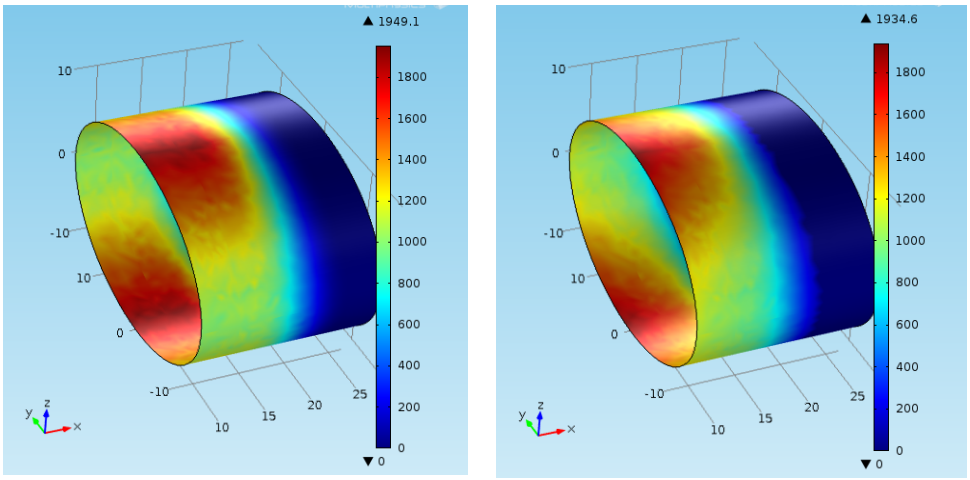

(a) (b)

Figure 4.11: Interface pressure for (a) cylindrical and (b) tapered balloon

When analyzing surface tissue data, the cylindrical balloon has an average interface pressure of 660 Pa, and a total interface force of .682N. The tapered balloon has an average interface pressure of 575 Pa, and a total interface force of .590 N. While both balloons showed complete sealing in this model, the cylindrical balloon once again appears to produce a better seal, due to its higher average

pressure and total interface force. Additionally, it has a larger surface area in contact with the chamber opening. Once again, these results indicate the cylindrical balloon provided better sealing to this chamber opening.

Principal strains were analyzed in all directions. Maximum principal strain at any point on the balloon was .052 for both models. While higher than strains encountered with circular chamber openings, it was still well below .2. This confirms that the linear elastic model is once again accurate for this balloon model.

Experimental testing

The main shortcoming of the previous balloon models is that the models have not addressed the high degree of geometric variability in chamber opening. As a result, it has been necessary to experimentally validate the ability of balloons to isolate the LAA from the left atrium. To test this, two different trials were used. The first looked at the balloon's ability to keep fluid from the LA from leaking into the LAA. The other tested the ability of the balloon to prevent hydrogel from leaking out of the LAA prior to solidification.

For each experiment, Braun International Impact Balloon Dilatation Catheters, with diameters of 20 mm each, were used (image shown below). These catheters are geometrically similar to the cylindrical balloon design modeled previously. Additionally, pig hearts were used, due to their wide availability and similarity to human hearts. In each trial, for easy access to the LAA, the heart was

cut open in the Left Ventricle. A catheter was inserted in this opening, and it travelled through the ventricle into the LA. Once in position at the opening of the LAA, the balloon was inflated to a pressure of 6 atm to isolate the appendage.

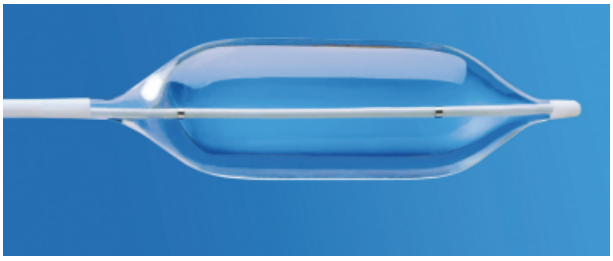

(a)

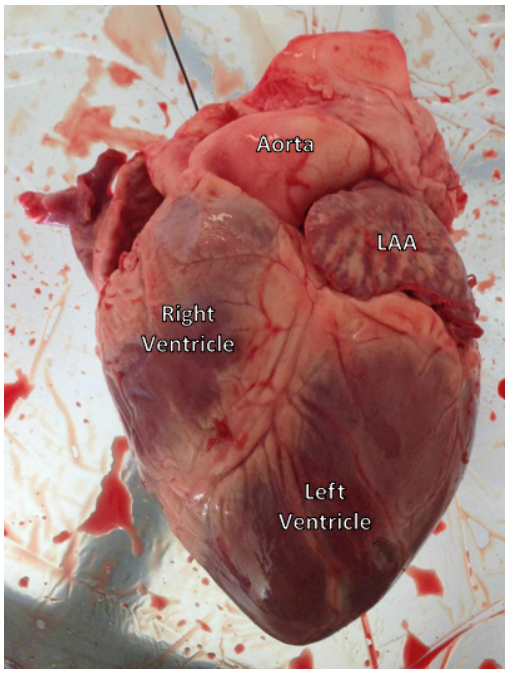

(b)

Figure 4.12: Braun International Balloon Dilation Catheter (a), and pig hearts (b), used during experimentation

Once the balloon was inflated, the heart was submerged in water to a depth of 34 cm. This depth creates a hydrostatic pressure of 25 mmHg, an upward limit for observed blood pressure encountered in the Left Atrium [4h]. Hearts were submerged at this depth for 5 minutes. After the elapsed time, hearts were removed, and any fluid that leaked into the chamber was removed, measured, and recorded. To simulate geometric variety, 6 separate pig hearts were used. Results from each trial can be seen in Table 4.2 below.

Table 4.2 Results from balloon isolation trials

Trial	Leakage (cm^3)	Leakage Flow Rate (µL/s)
1	.6	2
2	.24	.667
3	1.12	3.73
4	.15	.5
5	1.0	3.33
6	1.57	5.23
Average	.78	2.6

As seen in the table above, many of the trials have demonstrated significant fluid leakage into the appendage. Additionally, there was a large degree of variation in terms of leakage. This was likely caused by variation in chamber openings, as each pig heart has a unique LAA geometry. The balloon appeared to be more effective at isolating openings that were closer to being circular in shape. Additionally, larger LAA openings, (encountered on larger pig hearts tested), tended to have more leakage as well. This indicated that a larger balloon could be used in some situations to improve sealing.

While leakage into the appendage is an undesired result, it can be addressed by providing additional suction to the chamber. Average leakage rate for all trials was relatively small, and an order of magnitude smaller than expected flow rate during blood removal phase of the occlusion procedure. This indicates it would be possible to apply some sort of continual suction after the chamber is drained initially, negating the effects of any leakage into the chamber. It should also be

noted that the pressure outside the balloon for these trials represented an upward limit for pressure in the LA. This was done intentionally, to test the balloon under the most rigorous conditions. In a more realistic case

The next test examined the catheter balloon's ability to keep hydrogel components within the LAA. As in the previous trials, pig hearts and balloon dilatation catheters were used for this study. In each trial, the heart was filled with 5mL of water, and sealed with the balloon catheter. After sitting for 5 minutes, the balloon was deflated, and any fluid remaining in the chamber was removed, measured, and recorded. Results from this study were shown in Table 4.3 below.

Table 4.3: Results from trials for leakage out of the LAA

Trial	Leakage (cm^3)	Leakage Flow Rate (µL/s)
1	.12	.4
2	.05	.17
3	.22	.73
4	.04	.13
5	.18	.6
6	.35	1.17
Average	.16	.53

Leakage out of the chamber, while significantly less than leakage into the LAA, was still present in these trials. It was likely slower due to a lack of pressure being applied to the fluid under examination. As with previous trials, there is a high degree of variability for different hearts. While leakage of hydrogel out of the LAA can be dangerous to the patient, the amount encountered in these trials is not concerning to overall procedural success for two reasons. First, pressure outside

the chamber will likely be larger than pressure in the LAA, minimizing fluid flow out of the appendage. Additionally, it is possible to position the patient at an angle during the surgical procedure, causing the bottom of the LAA to be at a lower position than the opening. This would cause fluid to naturally flow deeper into the appendage, further reducing leakage out of the LAA.

As seen with both experiments, there is some leakage when the balloon is inflated. However, this leakage is small enough that is should not be a hindrance to successful occlusion, as will be demonstrated in a later chapter.

Conclusion

A three dimensional model was constructed to analyze interaction between the catheter balloon and the opening of the LAA. This model looked at two separate geometries for the balloon, as well two different appendage openings. In all scenarios, the balloon could form contact around the complete circumference of the chamber.

Experimentation was done with pig hearts and catheters to validate the models described above. While there was some leakage observed during experimentation, it could be addressed with additional suction, or positioning of the patient. This indicates that a catheter balloon can successfully isolate the LAA during the entire occlusion procedure.

Chapter 5: Mixing of Hydrogel Components

In order for solidify all hydrogel components, the two aqueous hydrogel solutions must be mixed completely. To account for fast hydrogel setting time, this mixing must occur at the delivery site. This chapter looks at potential mixing chamber designs and examines if a catheter tip mixing chamber can mix hydrogel components fully.

System Geometry and Entrance Region

To test the efficacy of various mixing chambers, three separate designs were modeled in COMSOL. Geometric specifications for these chambers were determined based on the design requirements of the medical device. The chamber must be no longer than 12mm in length, and must fit into a diameter of 3mm (due to this chamber being designed to go at the end of a cardiac catheter). This resulted in nominal cross section dimensions for each mixing chamber to be 1mm x 1mm.

The first design examined was a microgroove chamber. This was a straight channel, with rectangular raised groove on one wall as shown in Figure 5.1a. The next chamber design used geometric obstacles and barriers to redirect flow. The design includes flow redirectors on the walls, as well as obstacles through the central portion of the flow as shown in Figure 5.1b. The final design evaluated in this study was a 3D, serpentine chamber. Three-dimensional bends were chosen to induce transverse flow in all directions, creating more chaotic advection than a traditional 2D serpentine chamber. (Figure 5.1c).

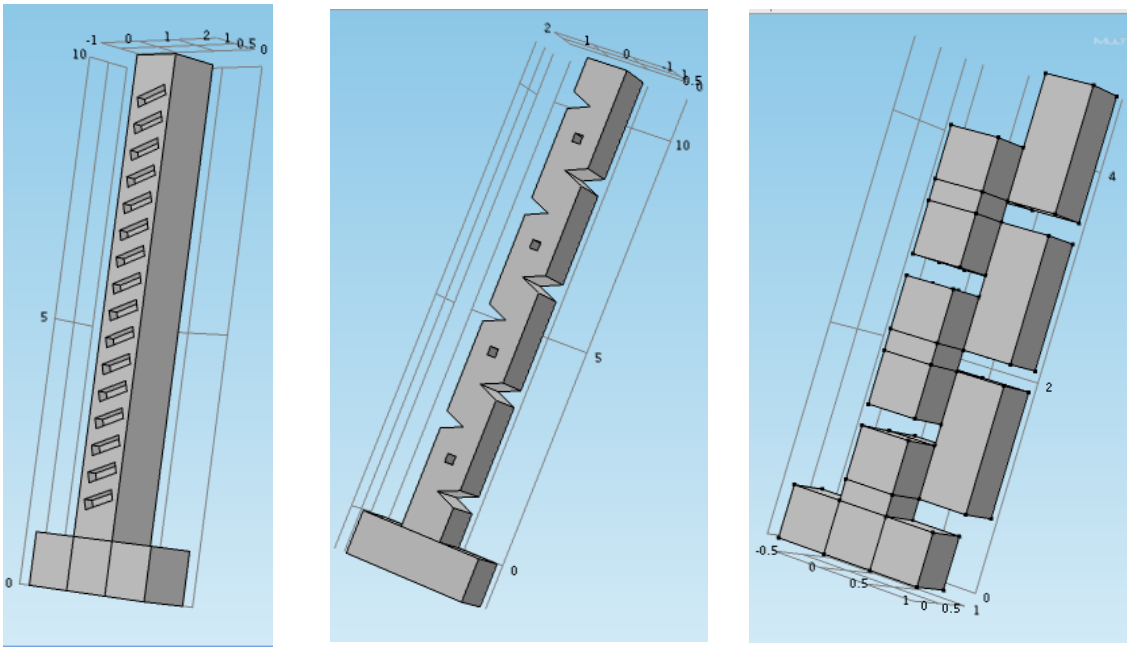

(a) (b) (c)

Figure 5.1: Mixing chamber designs investigated in this study: (a) diagonal microgroove, (b) geometric barriers, (c) serpentine.

It is worth noting that straight diagonal grooves are not the only type of wall modifications used for mixing in a microgroove mixing chamber. Herringbone patterns have also been shown to induce transverse velocity, and can often produce better mixing results. However, much of this efficacy is based on multiple cycles of switching herringbone patterns back and forth (Figure 5.2). This is necessary to catch and redirect flow throughout the chamber. In experimental work by Stroock *et al*, it was found that for a 100 μm chamber (1/10 of our chamber size), 15 cycles of switching (total length 3cm) were needed to mix flow completely [5a]. For a space-constrained application such as the one applicable in this study, this and other microgroove-based designs are not feasible for effective mixing.

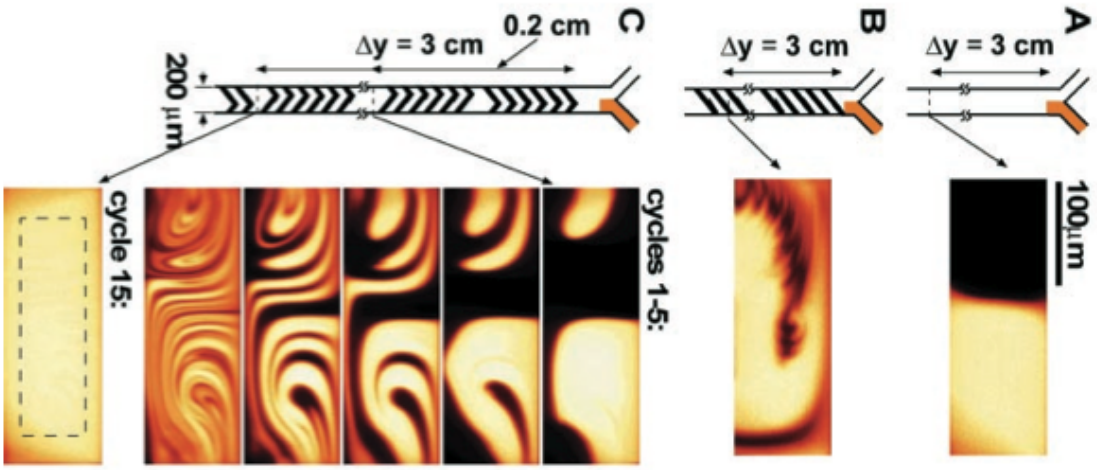

Figure 5.2 Qualitative depiction of mixing within a Herringbone pattern mixing chamber with multiple cycles [5a].

The entrance region dimensions and entry conditions for the flow were the same for all three chambers. The entrance region contains two entry points. One inlet feeds a PEG aqueous solution with the following mass fraction conditions: $\omega_{PEG} = 0.4,\ \omega_{DEX} = 0.0,\ \omega_{H2O} = 0.6$. The other inlet feeds a Dextran aqueous solution with the following mass fraction conditions: $\omega_{PEG} = 0.0, \omega_{DEX} = 0.4, \omega_{H2O} = 0.6$. Both inlets had a constant flow rate of 65 μL/s, which results in an average inlet velocity of 0.065 cm/s. The conditions specified above are shown schematically in Figure 5.3.

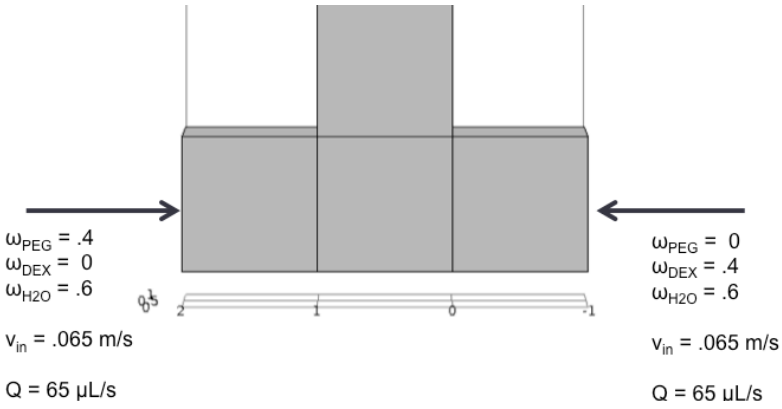

Figure 5.3: Entry region conditions specified for all three chambers.

Prior to performing the simulation, details about the fluid and mass transport models were investigated to ensure that the simulation accounted for the unique dimensionality and fluid interactions involved in this study.

Fluid Transport

Understanding the physical transport phenomena that occur in a microfluidic mixing chamber is a critical part of determining its design parameters and performance characteristics. Most micromixers have length scales ranging from micrometers to centimeters, thus allowing for a continuum analysis rather than a molecular treatment of the transport phenomena [5b]. As expected, the transport mechanisms are governed by conservation equations for mass, momentum and energy, each one of which are partial differential equations that can be solved for field variables such as concentration or velocity.

The fluid transport portion of the laminar flow is governed by Navier-Stokes equations, shown below.

Continuity: $$\rho \nabla \cdot \boldsymbol{u} = 0 \tag{5.1}$$

Momentum: $$\rho(\boldsymbol{u} \cdot \nabla)\boldsymbol{u} = \nabla \cdot [-p\boldsymbol{I} + \mu(\nabla \boldsymbol{u} + (\nabla \boldsymbol{u})^T)] + \boldsymbol{F} \tag{5.2}$$

In these equations, $\rho, \boldsymbol{u}, p, \mu, and\ \boldsymbol{F}$ are density, velocity, pressure, viscosity and effects of magnetic and electrical forces. This study assumes a laminar and incompressible flow, which will be solved for a steady state solution. A no-slip boundary condition is applied throughout the mixing chamber. Each chamber is expected to have a Reynolds Number range of Re < 10.

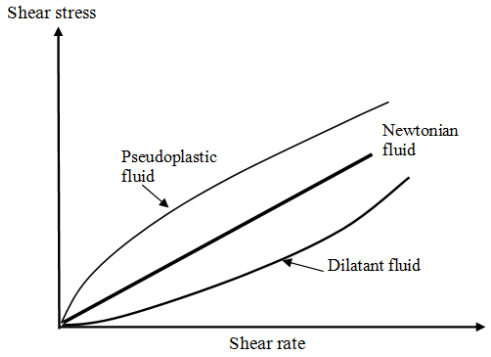

Figure 5.4: Stress-strain relationships for various types of fluids [5c].

Most polymeric solutions will exhibit non-Newtonian behavior at low shear rates similar to common shear-thinning, pseudoplastic materials as shown in Fig. 5.4. This would lead to a variable viscosity, which can often be modeled using a simple power law relation,

$$\mu_{eff} = K\left(\frac{\partial u}{\partial y}\right)^{n-1} \tag{5.3}$$

where K is the flow consistency index and n is the flow behavior index, which is less than one for a pseudoplastic material [5d]. However, the small dimensionality of typical micro channels along with the velocity ranges applicable to this study indicates that a Newtonian approximation may be possible given higher shear rates. This approximation is supported by the work of Gonzalez-Tello *et al* which examined the variation of dynamic viscosity for concentrated PEG aqueous solutions at various concentrations, molecular weights and shear rates. Figure 5.5 shows that for a PEG solution at 40% concentration and various molecular weights, the viscosity is nearly constant for a shear rate range of 200 s^{-1} to 1,300 s^{-1} [5e]. Therefore, a Newtonian behavior has been assumed for simulation purposes.

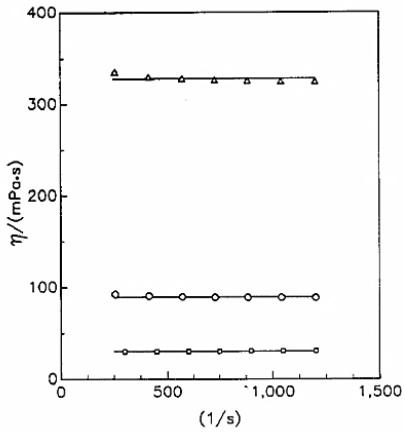

Figure 5.5 Influence of shear rates on the viscosity, η, for w(PEG)=0.40 at 277 K: (Δ) PEG8000; (○) PEG 3350; (□) PEG 1000 [5e].

The viscosity and density values for the PEG and Dextran solutions were obtained from past experimental work for this study and are shown in Tables 2.1 and 2.2. Although the simulation assumes a incompressible flow with Newtonian behavior, the viscosity and density still varies based on the mass fraction of each material present at a given solution point. The equation below provides the value of

viscosity (Pa-s) as a function of the mass fraction of each material present at a given point. A similar equation provides a relationship for the density (kg/m^3). In both equations, ω_{PEG} and ω_{DEX} represent the mass fraction of PEG and Dextran respectively. These relations were implemented into the COMSOL environment for each simulation.

$$\mu = 0.0328\times\left(\frac{\omega_{PEG}}{\omega_{PEG}+\omega_{DEX}}\right)+0.0165\times\left(\frac{\omega_{DEX}}{\omega_{PEG}+\omega_{DEX}}\right) \tag{5.4}$$

$$\rho = 1393\times\left(\frac{\omega_{PEG}}{\omega_{PEG}+\omega_{DEX}}\right)+1399\times\left(\frac{\omega_{DEX}}{\omega_{PEG}+\omega_{DEX}}\right) \tag{5.5}$$

Determination of Ternary Maxwell-Stefan Coefficients

In theory, using ternary Fick diffusion coefficients and how they change with concentration for a given system, one could obtain the corresponding MS diffusivities. However, there is very little previously published data for experimentally measured ternary diffusivities. For most systems, the only measured diffusion coefficient data that can be found are the binary Fick diffusion coefficients. Where ternary system data does exist, it is very rarely over the entire concentration range of the system, giving it limited value for this study. It is therefore necessary to predict the ternary Maxwell-Stefan diffusion coefficients over a given system's entire concentration range using data on the binary Fick coefficients of the three binary subsystems of which compose this system.

Vignes previously developed a model which predicts the binary MS diffusion coefficients for a given system over its entire concentration range based on knowledge of the corresponding Fick diffusivities at infinite dilution [5f]:

$$Đ_{12} = (D_{12}^{x_2 \to 0})^{x_1} \cdot (D_{12}^{x_1 \to 0})^{x_2} \tag{5.6}$$

The ternary MS diffusivities are then predicted from the binary MS diffusivities using a ternary extension of the Vignes equation [5g]

$$Đ_{ij} = (Đ_{ij}^{x_i \to 1})^{x_i} \cdot (Đ_{ij}^{x_j \to 1})^{x_j} \cdot (Đ_{ij}^{x_k \to 1})^{x_k} \tag{5.7}$$

While the first two MS binary coefficients at infinite dilution are known from Vignes equation, the third term is unknown and must be modeled. To predict this final term, in their paper, Rehfeldt and Stichlmair proposed a model that is a combination of the approaches taken by Wesselingh & Krishna and Kooijman & Taylor [5g].

$$Đ_{ij} = (Đ_{ij}^{x_i \to 1})^{x_i} \cdot (Đ_{ij}^{x_j \to 1})^{x_j} \cdot (Đ_{ij}^{x_i \to 1} \cdot Đ_{ij}^{x_j \to 1} \cdot Đ_{ik}^{x_k \to 1} \cdot Đ_{jk}^{x_k \to 1})^{x_k / 4} \tag{5.8}$$

Using this model, Rehfeldt *et al* achieved an average deviation of 23.9% when predicting ternary diffusion coefficients for the system acetone – 1- butanol – 1-propanol.

Obtaining MS Diffusivities for PEG-DEX-H_2O

The system being considered for occlusion of the LAA consists of an 11 kilo Dalton (kD) polyethylene glycol (PEG), 11 kD Dextran, and liquid water. Denoting water as species 0, PEG as species 1, and Dextran as species 2, the binary infinite dilution coefficients at 313 K obtained from the literature are given in Table 5.1.

Table 5.1: Binary Fick diffusion coefficients at infinite dilution [m²/s] [5h, 5i, 5j]

$D_{01}^{x_0 \to 0}$	$D_{01}^{x_1 \to 0}$	$D_{02}^{x_0 \to 0}$	$D_{02}^{x_2 \to 0}$	$D_{12}^{x_1 \to 0}$	$D_{12}^{x_2 \to 0}$
1.0×10^{-12}	1.76×10^{-10}	2.0×10^{-12}	5.0×10^{-10}	1.5×10^{-12}	1.5×10^{-12}

Some approximations had to be made where exact data was not available from literature. Chin *et al* [5h] measured the infinite dilution diffusion coefficient of PEG in water as a function of molar mass of PEG at 313 K. They showed a power law could describe this relationship very accurately:

$$LogD = -0.37 logM - 8.26 \tag{5.9}$$

Here, M is the molecular mass of the PEG [g/mol] and D is the binary Fick diffusion coefficient [m²/s] at infinite dilution. Using the equation above, the infinite dilution diffusion coefficient of 400 g/mol PEG in water was converted to a value for this coefficient for 11 kD PEG (shown as the second entry in Table 5.1 above). Trampel *et al* measured the diffusion coefficients of Dextran and PEG in water at various concentrations and molecular weights [5j], and this data was extrapolated to the concentration extremes of each binary system in order to obtain infinite dilution coefficients.

The binary Fick diffusion coefficients at infinite dilution given in Table 5.1 were used in the equation from Vignes to compute the binary Maxwell-Stefan diffusivities as functions of species concentration. These values were then used to compute the three independent ternary Maxwell-Stefan diffusion coefficients over the entire concentration range of the PEG-Dextran-water system. These diffusivities

are given in the equations below and were imported into the COMSOL models to allow for the accurate calculation of species diffusion.

$$Đ_{01} = (1E^{-12})^{x_1}(1.76E^{-10})^{x_0}\left[(1E^{-12})(1.76E^{-10})(2E^{-12})(1.5E^{-12})\right]^{x_2/4} \quad (5.10)$$

$$Đ_{02} = (2E^{-12})^{x_2}(5E^{-10})^{x_0}\left[(2E^{-12})(5E^{-10})(1E^{-12})(1.5E^{-12})\right]^{x_1/4} \quad (5.11)$$

$$Đ_{12} = (1.5E^{-12})^{x_2}(1.5E^{-12})^{x_1}\left[(1.5E^{-12})(1.5E^{-12})(1.76E^{-10})(5E^{-10})\right]^{x_0/4} \quad (5.12)$$

Results

Optimal crosslinking for PEG and Dextran occurs when the two are mixed in a 1:1 mole ratio. Because the substances have similar molecular weights (~11,000 g/mol), optimal mixing occurs when the $\omega_{PEG} = \omega_{DEX}$. This study's quantitative mixing analysis looks at the difference between these two mass fractions. To evaluate mixing conditions, a plane normal to the flow chamber was designated at the exit region, as shown in Figure 5.6 below. At all locations in this plane, mass fraction data for PEG and Dextran were exported to MATLAB for further analysis.

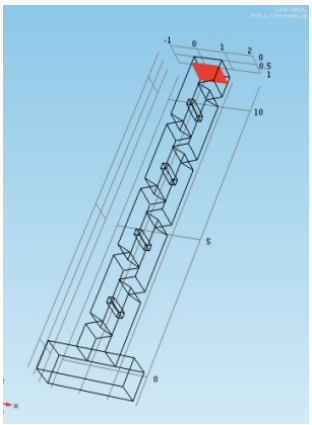

Figure 5.6: Diagram showing exit-region cross section used for evaluation.

Statistical methods were used to quantify the amount of mixing in each chamber. A normalized histogram was made for PEG and DEX mass fraction difference at the exit region. A PDF based on this histogram was then constructed to determine the probability of a given mass fraction difference at any point. Mixing Efficiency, ME, was defined with the following equation:

$$Mixing\ Efficiency = ME = 1 - \sqrt{\frac{1}{N}\sum_{i=1}^{N}(\Delta_i - \bar{\Delta})^2} \qquad (5.13)$$

Where Δ_i = mass fraction difference of PEG and Dextran at the i^{th} location, Δ = mean of mass fraction difference for the data set, and N = total number of recorded data points in the domain. Mixing efficiency is 1 if the two fluids are fully mixed and 0 if there is no mixing [5k].

Mass fraction data for the microgroove mixing chamber are shown in the figures below.

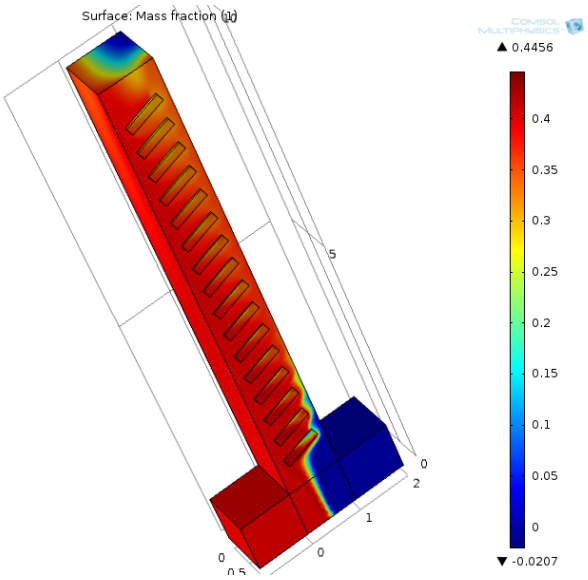

Figure 5.7 PEG mass fraction for the microgroove mixing chamber.

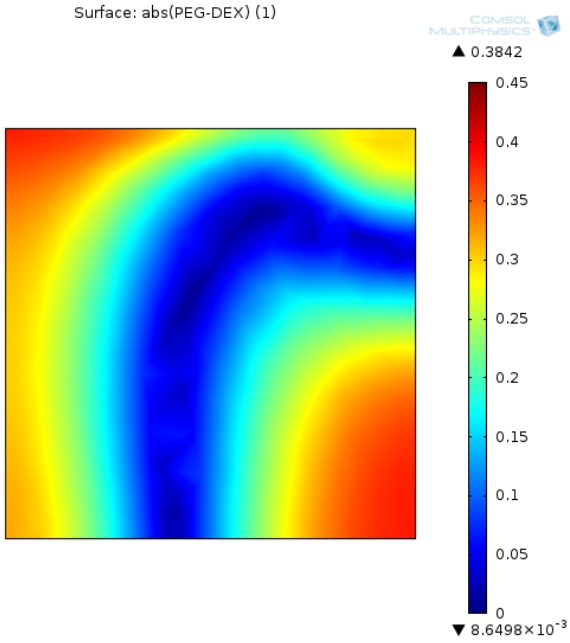

Figure 5.8: Difference between PEG and Dextran mass fractions at exit region of the microgroove mixing chamber.

As shown in Figures 5.7 and 5.8, there is a small region of well-mixed material using the microgroove design; however, a majority of the fluid maintains a high mass fraction disparity. The chamber was able to induce some chaotic

advection due to flow redirection around the grooves, but in its current form, requires more length to achieve the desired level of mixing of the two polymers at the exit plane.

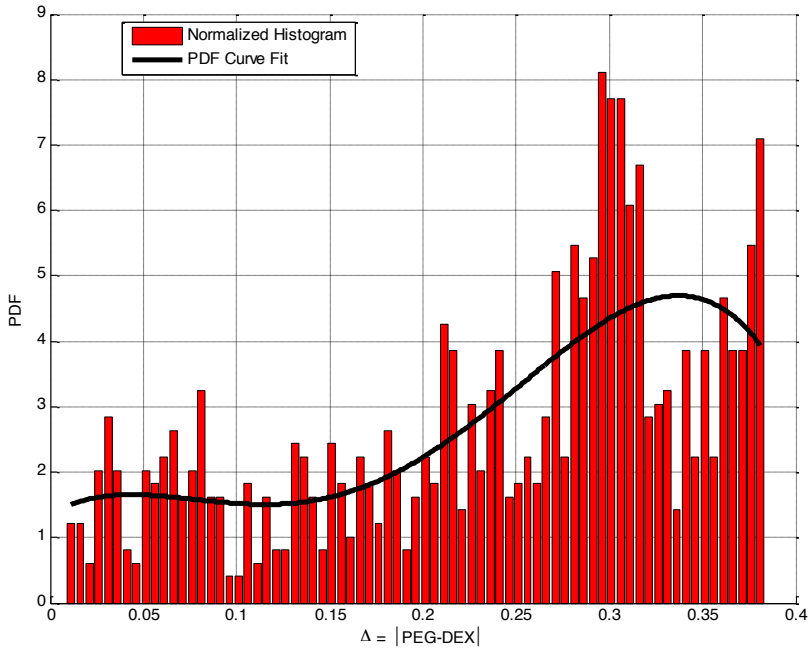

Figure 5.9: Histogram and PDF quantifying mass fraction difference of PEG and DEX in the microgroove mixing chamber

The histogram shown in Figure 5.9 gives a quantitative picture of the degree of mixing within the fluid at the exit plane of the microgroove. The mixing efficiency is a relatively poor 0.74, and the histogram is skewed to the right indicating low mixing within a large portion of the flow. Only 16% of the fluid is mixed to such a degree that the mass fraction differential is within 0.10.

Mass fraction data for the Geometric Barrier chamber are shown in the figures 5.10 and 5.11.

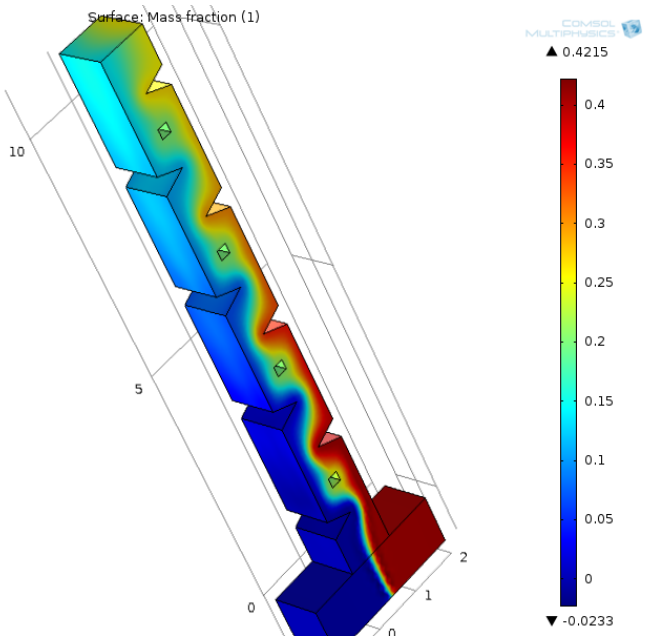

Figure 5.10: PEG mass fraction for the geometric barriers mixing chamber.

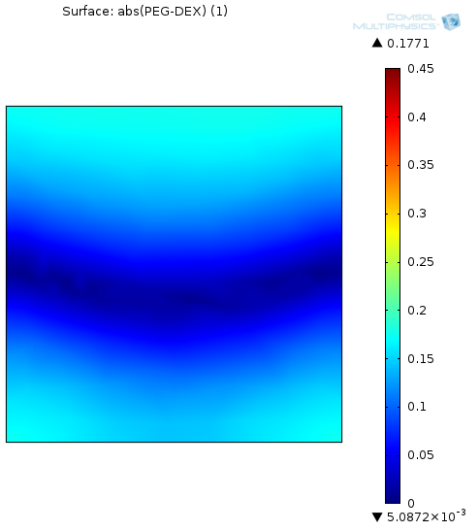

Figure 5.11: Difference between PEG and Dextran mass fractions at exit region of geometric barriers mixing chamber.

From Figures 5.10 and 5.11, the geometric barriers mixing chamber is significantly more effective at mixing than the microgroove chamber. The entire flow at the exit plane is mixed to within less than a 0.178 disparity in mass fraction between PEG and Dextran. There was also notice a large streak down the middle of

the flow field where there is essentially no difference at all in the mass fraction of the two polymers indicating near perfect mixing.

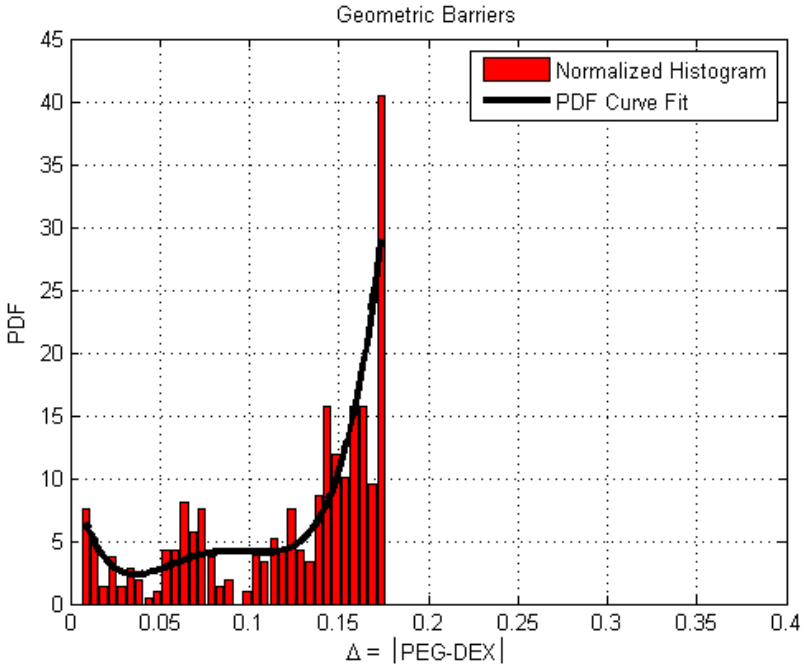

Figure 5.12: Histogram quantifying mass fraction difference of PEG and DEX in geometric barriers mixing chamber.

The histogram shown in Figure 5.12 confirms the effectiveness of the geometric barriers mixing chamber. No region of the fluid exhibits a mass fraction disparity greater than 0.125. The mixing efficiency for this chamber is ME = 0.867, and 60% of the flow passing through the exit plane is mixed to within a 0.10 mass fraction difference between PEG and Dextran. It appears that the direct obstruction to the closed by the wedges and vertical columns of the geometric barrier are effective at inducing transverse flow motion. By maintaining a periodic cycle of these obstacles, the chamber is able to accomplish mixing in a spatially efficient manner.

Mass fraction data for the serpentine mixing chamber are shown in the figures below.

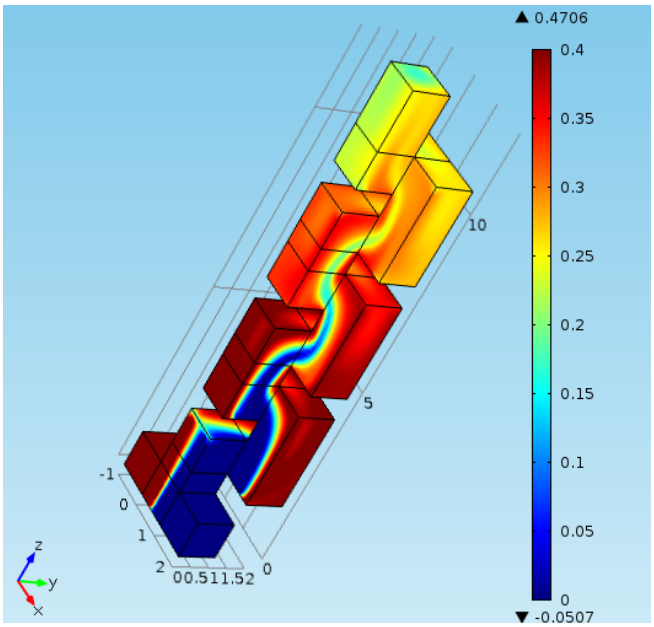

Figure 5.13: PEG mass fraction for the serpentine mixing chamber.

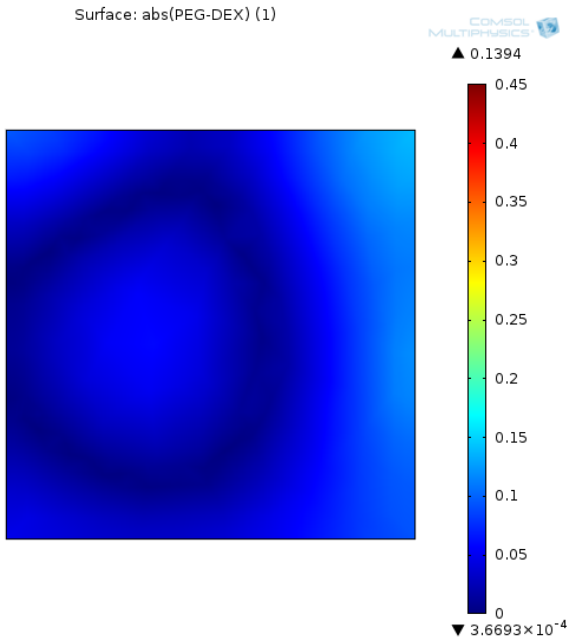

Figure 5.14: Difference between PEG and Dextran mass fractions at exit region of the serpentine mixing chamber.

As shown in Figures 5.13 and 5.14, the serpentine mixing chamber is more efficient in the mixing process than the microgroove based mixing chamber. While there are some regions near the outer walls that exhibit a mass fraction disparity between PEG and Dextran, the majority of the fluid is relatively well mixed. As expected, the deliberate redirection of the flow using repeated 90° bends increases the transport characteristics in the transversal direction leading to more efficient mixing.

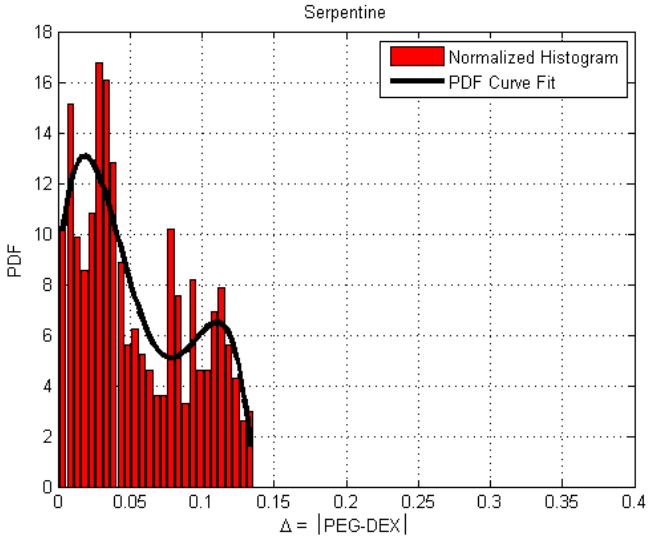

Figure 5.15 Histogram and PDF quantifying mass fraction difference of PEG and DEX in the serpentine mixing chamber.

The histogram shown in Figure 15 indicates that the serpentine chamber produces the best overall mixing. Relative to the microgroove mixing chamber, this histogram shows a higher degree of mixing as indicated by a slight skew to the left. The mixing efficiency parameter confirms this with a value of ME = 0.944, the highest Mixing Efficiency of all three chambers. At the exit plane of this serpentine

mixing chamber, all fluid is mixed to within a 0.139 mass fraction difference between PEG and Dextran.

Figure 5.16 provides a comparison of the PDF and exit region profile for all three chamber designs. Qualitatively it is clear that the mixing process improves significantly from the microgroove design to the serpentine design. In addition, a comparison of the PDFs shows that the distribution is contracting towards a zero difference between the mass fraction of PEG and DEX when using a serpentine design.

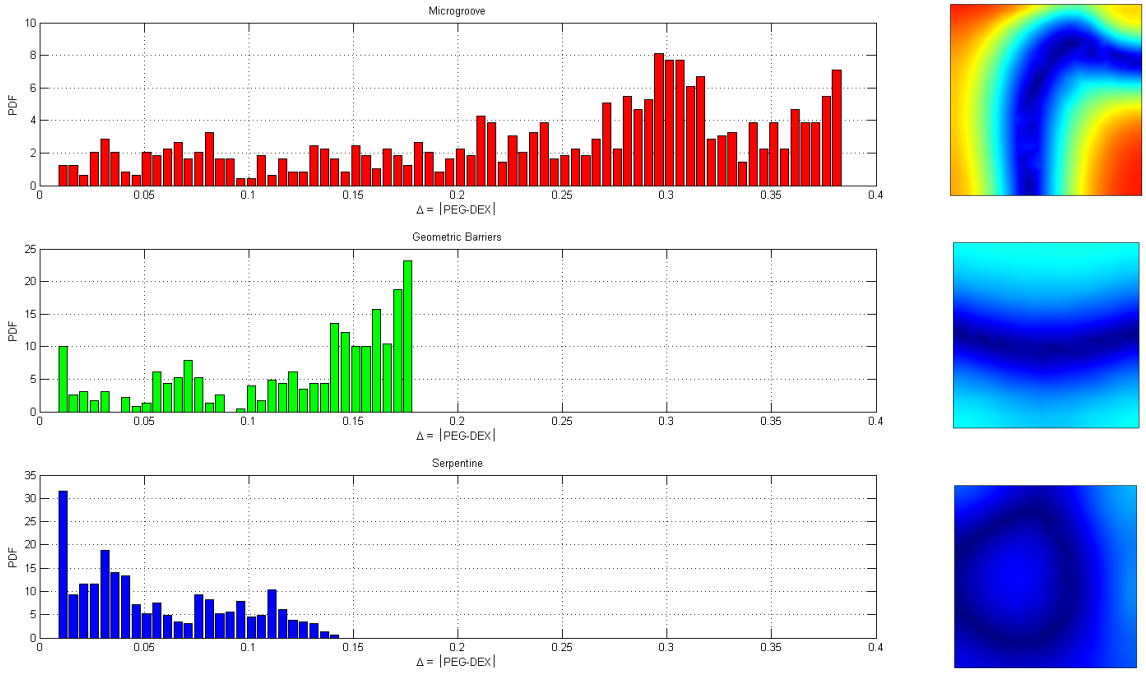

Figure 5.16: Comparison of PDFs and exit region profiles for all three chamber designs

One concern that arose for this mixing is inconsistent fluid velocity. Because hand force from the surgeon is the source of driving pressure for hydrogel

components, fluctuations in pressure or flow rate could occur. This could have a significant effect on chaotic advection and overall mixing for the chamber. To analyze this hypothetical situation, all three models were run for multiple inlet velocities. While both inlets still maintained the 1:1 ratio for fluid velocity, this velocity was tested from .045-0.85 m/s, increasing in increments of .05. ME values for varying fluid velocities are shown in Figure 5.17 below.

Both the Serpentine and Geometric Barriers chamber have an ME value that increases with increasing flow rate, with the serpentine chamber having a larger variability. However, for all inlet velocities, the Serpentine chamber still has the highest ME value. The Microgroove chamber, however, shows a decreasing ME value. However, variation in ME is very small, and mixing is almost consistent with this chamber for all inlet velocities.

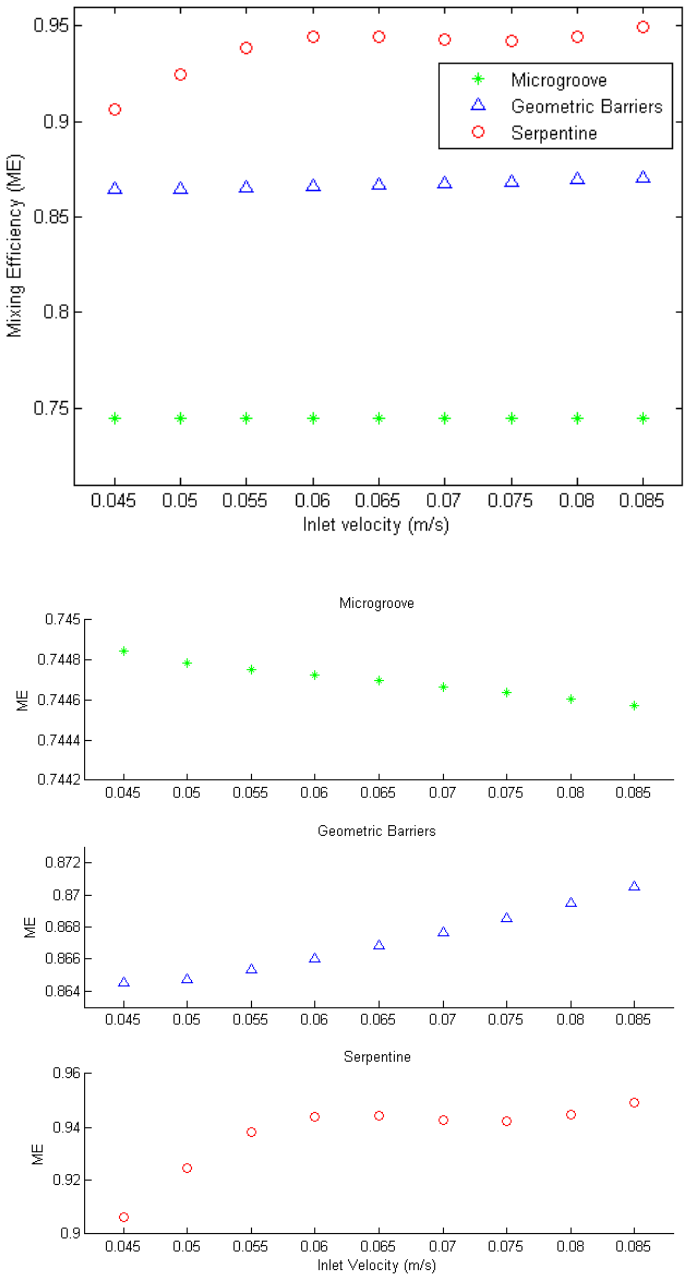

Figure 5.17a and b: ME values for varying entry region flow rates for all three mixing chambers.

Experimental Testing of chamber

To test the validity of the previous model, a physical prototype was made of the serpentine mixing chamber. This chamber was fabricated out of nylon using Selective Laser Sintering. Due to manufacturing constraints, this prototype was a

4:1 scale model of the actual mixing chamber. Additionally, to prevent undesired fusing of powder in the mixing channel, the chamber was manufactured in two halves, and reassembled with pins. Figure 5.18 below shows the prototype chamber

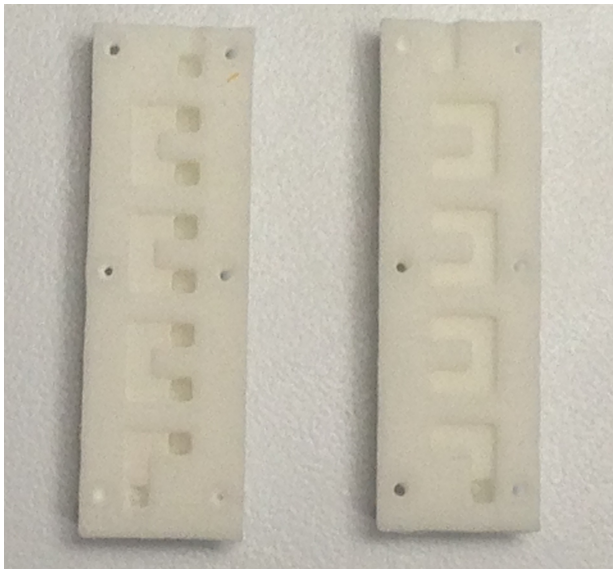

Figure 5.18: Halves of mixing chamber made out of SLS

To simulate the hydrogel components, Loctite Heavy Duty Epoxy (product number 1172794) was used. Like the candidate hydrogel material, it is made of two components, and is ideally mixed in a 1:1 ratio. Additionally, this epoxy sets relatively quickly, and can be used to evaluate if a prototype chamber mixes fluids completely. This makes it a suitable, inexpensive material for testing this mixing chamber.

To ensure this testing was an accurate evaluation of the proposed chamber design, a dimensional analysis was performed. Buckingham Pi Theorem was used to

ensure accurate similitude analysis. The system has 13 parameters, and can be defined as:

$$F = f(D_A, D_B, \omega_A, \omega_B, \Delta\omega, U_A, U_B, \rho_A, \rho_B, \mu_A, \mu_B, L, w) \tag{5.14}$$

A description of all parameters can be seen in Table 5.2 below. It is important to note that in this model only two diffusion coefficients – infinite dilution for both hydrogel components– were included in this analysis. This simplification was done out of necessity, as extensive diffusion data was not available for this test material. Previous research into this material has focused primarily on fluid properties, and diffusion of the epoxy has not been investigated in depth. When Buckingham Pi method is completed, the following relation emerges:

$$\frac{\Delta\omega}{\omega_A} = f(Pe, Re, \frac{\omega_B}{\omega_A}, \frac{U_B}{U_A}, \frac{\mu_B}{\mu_A}, \frac{w}{L}, \frac{\rho_B}{\omega_A}) \tag{5.15}$$

In the equation above, Pe and Re denote Peclet Number and Reynolds Number, respectively. These two terms are defined as follows:

$$Pe = \frac{U_A L}{D_B} \tag{5.16}$$

$$Re = \frac{\rho_A U_A L}{\mu_A} \tag{5.17}$$

Knowing this relation, dimensions for prototype testing can be determined. Table 5.2 below shows values used in the model, as well as their similitude values for prototype testing [5d 5L].

Table 5.2: Variable description and values used for similitude prototype testing

Variable	Description	Model	Prototype	Dimension
w	Width of chamber	1	4	mm
L	Length of fluid travel	22.5	90	mm
D_{ia}	Infinite dilution coefficient of PEG	1.76E-10	4.50E-10	cm^2/s
D_{ib}	Infinite dilution coefficient of DEX	5.00E-10	4.50E-10	cm^2/s
ω_a	Initial mass fraction of PEG	0.4	0.335	1
ω_b	Initial mass fraction of DEX	0.4	0.335	1
U_a	Inlet velocity of PEG	0.065	0.01	m/s
U_b	Inlet velocity of DEX	0.065	0.01	m/s
ρ_a	Density of PEG solution	1393	1040	kg/m^3
ρ_b	Density of DEX	1399	1170	kg/m^3
μ_a	Viscosity of PEG solution	32.8	15.1	cP
μ_b	Viscosity of DEX solution	16.5	7.6	cP

Once experimental values were known, it was possible to test the prototype mixing chamber. The mixing chamber was assembled, and a syringe was attached to each entry region to control PEG and DEX flow rate. To prepare epoxy, components were diluted to the proper concentration and density with denatured alcohol. Next, trace amounts of baking soda were added to both the resin and hardener to bring components to the desired viscosity. While this adds another transported component to the testing fluid, it should not have a large effect on the epoxy. Mass fraction of baking soda was <.001 in all cases, and was small enough to be negated for this experimentation. Additionally, it was necessary to modify viscosity to maintain dimensional similarity, due to the large number of variables in this analysis.

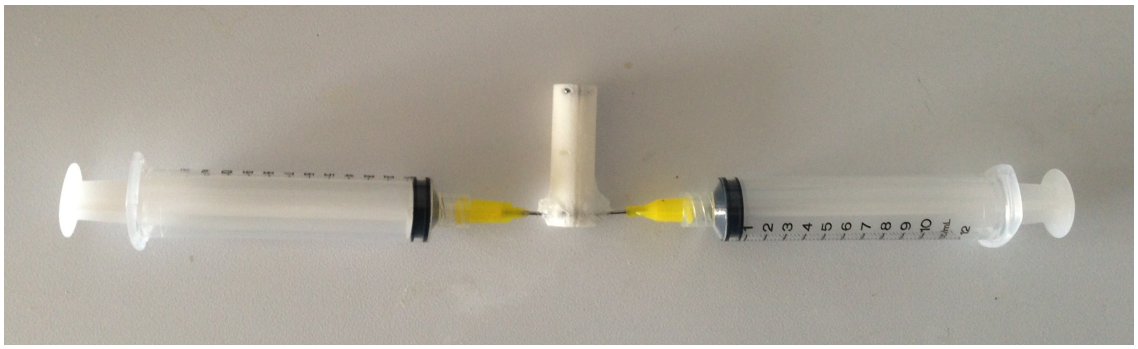

Figure 5.19: Assembled mixing chamber and syringes used for testing

For each trial, epoxy resin and hardener were prepared as described above, and mixed in the prototype mixing chamber in a 1:1 ratio. Mixed components were placed in a vial, and allowed to sit for 5 minutes (the working set time for the epoxy used). 10 total trials were completed for this experiment.

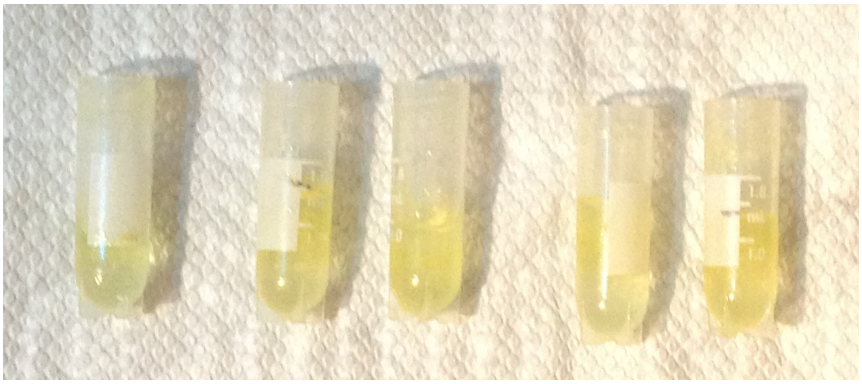

Figure 5.20: Vials of solidified epoxy mixed by prototype mixing chamber

For 8 of the 10 trials, all material within the vial solidified after 5 minutes without incident. In two other vials, most of the epoxy had solidified, with some material at the top of the vial still in liquid form. The two remaining vials were allowed to sit for 5 additional minutes, at which point, all remaining material had solidified. In these two trials, slow curing can likely be attributed to human error. Due to syringe configuration, it was difficult to pump both epoxy components in a

1:1 ratio, and there was a noticeable disparity in epoxy component flow rate for the two trials mentioned above. In future applications, the likelihood of this error can be mitigated by using a dual-plunger syringe (shown in Figure 5.20 below) to keep flow rate of hydrogel components consistent. Allowing for additional time for solidification during an occlusion procedure can also help ensure complete solidification, in the event that this error does occur.

Figure 5.21: Dual plunger syringe

Conclusion

A model for mixing of hydrogel components was completed and presented in this chapter. This model utilized a ternary component diffusion model, and used fluid properties of hydrogel components determined previously. Three different mixing chambers were examined, and mixing was quantified to evaluate the chambers mixing ability. One design, a serpentine mixing chamber, stood out as the most effective for mixing hydrogel components. A prototype of this serpentine chamber was fabricated and tested as well. This prototype was able to mix an epoxy imitating the filling hydrogel, and results confirmed those from the model.

Chapter 6: Entire System Analysis

Up to this point, modeling and experimentation work has focused solely on individual subfunctions. However, it is important to understand how these subfunctions interact with each other and to verify that each one can be performed successfully within an entire catheter device. It will be one focus of this chapter to present this understanding and verification.

Function-Structure Diagram

To better promote understanding of the entire surgical occlusion process, the entire procedure has been mapped out in a Function-Structure diagram. This graphical representation takes all subfunctions into account, and delineates a network of all subfunctions that must be completed for successful occlusion. The diagram also tracks energy, material, and signal movement throughout the entire medical device. Table 6.1 below lists all subfunctions that must occur during the surgical procedure, and the actual diagram is shown on the subsequent page [6a].

Table 6.1: Subfunctions Required for Surgical Procedure

Insert and position guide wire
Insert and position catheter
Isolate Appendage (with balloon)
Drain LAA
Transport hydrogel components to the LAA
Mix hydrogel components in the LAA
Deconstruct and remove device

Hand power (via manual direction and use of a syringe) is the primary energy source for the entire occlusion procedure. It is used to position the catheter,

drain fluid from the LAA, and transport and mix hydrogel components. Previous analysis has shown that hand power is sufficient for all with all the steps within the occlusion procedure. Additionally, this power source is one preferred by surgeons, and it gives them extensive control over all aspects of the occlusion procedure.

Some subfunctions must be done in a precise order such that some are completed before others can proceed. For example, the catheter must be positioned properly before the isolation balloon can be properly inflated. Additionally, the LAA must be completely drained before hydrogel components can be transported and solidified. The FS diagram demonstrates the need for reliable, real-time sensing throughout the entire occlusion procedure.

While not analyzed extensively in this research, fluoroscopic probes remain a likely candidate for monitoring the surgical procedure. Emitting x-rays, these probes can provide real time imaging within the body, and they have been used extensively in the past during catheter-based angioplasty and stent deployment procedures. Iodine-based contrast agents such as Isovue can complement imaging with these probes and have been previously inserted in the blood stream to diagnose blockages. Additionally, these agents can assist in viewing hydrogel components in both the liquid and solidified forms. These iodine molecules have a length of ~1-10 nm each, and they are easily able to fit in the mesh of solidified hydrogel. (While mesh size does vary with concentration and other properties, it is in the order of microns, thus meaning that iodine molecules can clearly fit). These

observations further support the use of iodine-based contrast agents for monitoring both the draining of the LAA, as well as the filling and solidifying of the hydrogel.

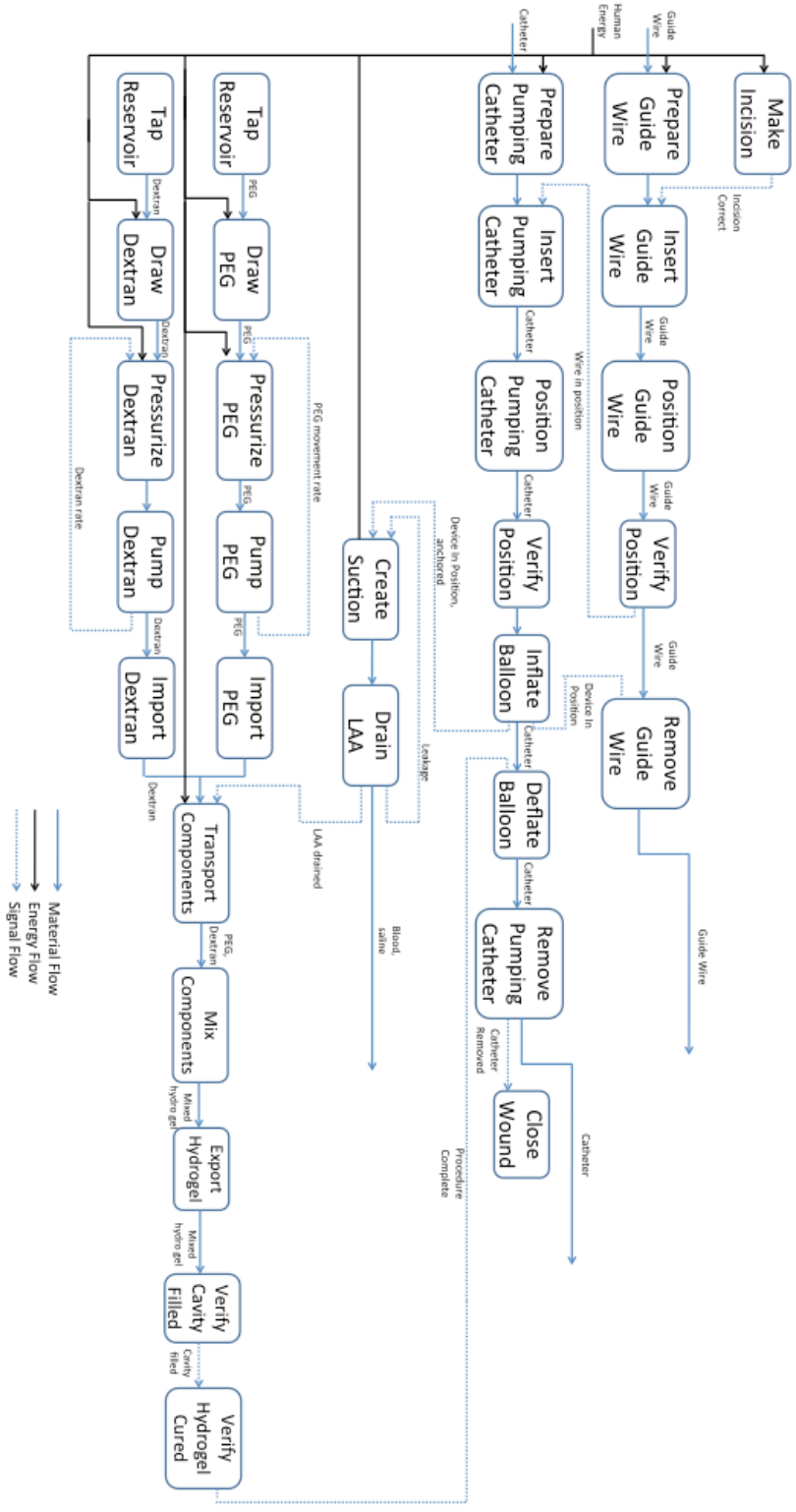

Figure 6.1: Function Structure Diagram for Entire System

Manufacturing of Device for Mass Production

It is important that all systems of the proposed device can be manufactured in a reproducible manner that will be certifiable by current FDA regulations. While a complete manufactured prototype was not completed for this research, potential manufacturing methods were analyzed. Research looked into manufacturing methods for all components, as well as the assembly of an entire occluding device.

Catheter tubing is often manufactured through plastic extrusion. For this process, thermoset or thermoplastic pellets are melted and pushed through a die to shape the tubing. Once extruded, tubing is cut down to size and inspected for quality. Most medical extrusion molding machines are able to work with custom dies that create the desired cross section. It is thus possible to manufacture most any catheter cross-section design. Almost all catheter tubing is made through this method, and there are many facilities approved for this manufacturing method.

Figure 6.2: Extruded multi-lumen catheter tubing [6b]

Catheter manifolds are an important part of the device as well, as they allow individual lumens to connect with other devices and components. This part would likely be produced and attached to tubing through insert molding. Previously extruded catheter tubing would be inserted into a mold, with melted plastic injected around this insert. This forms a tight, waterproof connection between the two parts. The technique described is used extensively for catheters, and many facilities are approved for this type of medical manufacturing.

Figure 6.3: Manifold connecting multi-lumen tubing to Luer Lock connections [6c]

Injection molding is a likely method for manufacturing the mixing chamber. This method allows for reproducibility and cost effectiveness in larger quantities. Additionally, there are multiple injection molding manufacturers approved for medical device manufacturing, and tolerances as small as .001 inches are possible. One challenge for producing the mixing chamber with this method is designing a

suitable mold for this chamber. The chamber cannot be manufactured in one piece, as it would be impossible to remove the finished piece from the mold. The internal channel would create overhang, making it impossible to remove without causing damage. By manufacturing the chamber in two pieces – that is, by dividing the internal chamber into two halves -- overhang can be eliminated. Figure 6.4 below shows two possible halves that could be assembled to form a complete mixing chamber. Multiple medical adhesives -- adhesives approved for *in vivo* usage with medical devices -- are available to assemble this chamber, as well as attach it to the catheter. Ultrasonic welding is also a viable assembly method used often for medical devices.

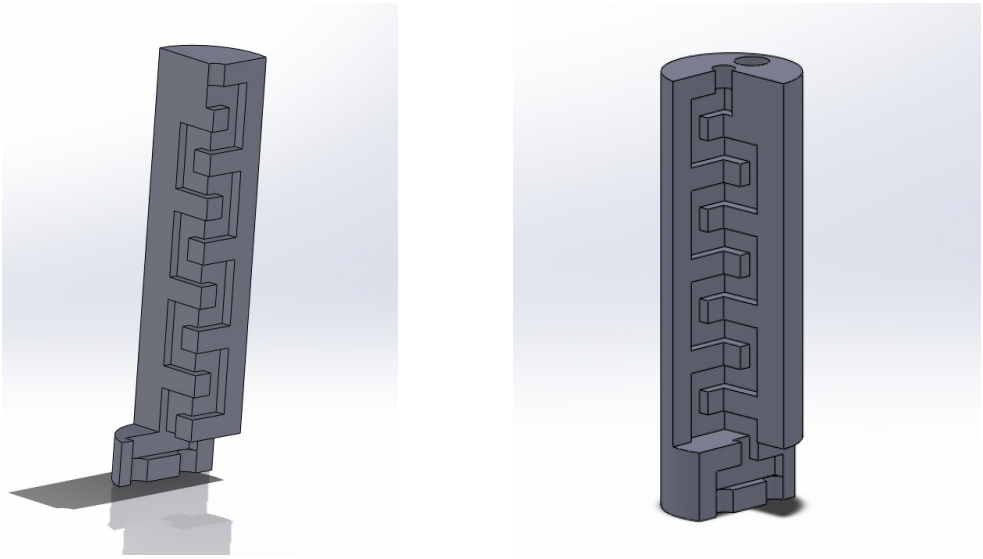

Figure 6.4: Halves of mixing chamber that can be assembled by injection molding

There are some additional design considerations, however, that must be taken into account when planning to manufacture a part via injection molding. Throughout the part, material thickness should be relatively consistent, to prevent

warping due to uneven shrinkage. The entry region of the mixing channel cannot be placed too close to the edge, for risk of creating a region of low part thickness. Additionally, to ease removal of the part from the mold, the flow chamber must have a draft angle of ~2 degrees. While it is very straightforward to incorporate these design constraints into a final mixing chamber design, this will affect how the chamber redirects flow as well as mixing that results from this redirection. Future work should take these design constraints into account, and focus on modeling a mixing chamber designed for injection molding manufacturing [6d].

FDA regulation for Manufacturing

It is also important to look at regulatory factors that can affect the guidelines for the manufacturing of a device. The FDA has outlined best practices for manufacturing, as well as guidelines for approved manufacturing facilities. Additionally, for some device regulatory categories, there are specific manufacturing requirements. Determining a likely FDA roadmap for this occluding device is important for evaluating the appropriateness of the manufacturing techniques discussed previously.

This invention would likely be considered and regulated as a Class III medical device. This is the most stringent regulatory class, and it covers all devices that pose a high risk to the patient receiving the treatment. Long term implants, like endossial implants and pacemakers, are almost exclusively regulated under this category. A

long-term hydrogel implant would likely receive similar classification. This classification is also applied to devices where there is insufficient data for safety and efficacy determinations based on previously approved devices. As there are few other devices that mix hydrogel components in the body, it will be difficult to establish a predicate device, the establishment of which is a necessary step for Class I and Class II classification. It seems most certain that Class III classification will be the expected assignment of this device [6e].

Class III medical devices must file and receive a Pre-Market Approval (PMA) -- a submission and approval required before marketing. This documentation primarily calls for testing that confirms the safety and efficacy of the device. However, it also must include "a complete description of the methods used in, and the facilities and controls used for, the manufacture… of the device" [6f]. This entails extensive documentation of plans for manufacturing, packaging, storing, and distributing the device. However, it does not limit the actual manufacturing methods, assuming adequate controls and quality standards can be established. All manufacturing methods discussed above have been used extensively for previous device manufacturing, and FDA regulations, which have been reviewed, should not add any further challenges to the manufacturing of this product.

Entire Fluid Transport Analysis

All previous fluid analysis has focused on individual subfunctions. However, all fluid transport and mixing must be conducted simultaneously for successful hydrogel delivery. As a result, it is necessary to test all fluid transfer functions at once.

To test the entire fluid transport process, a prototype that covered all steps of fluid movement was created. This prototype used the 4:1 scale serpentine mixing chamber described earlier in Chapter 5. Polyurethane tubing with an ID of 5.25 mm (approximately 4 times 1.3mm – the tubing diameter designated earlier for hydrogel component fluid flow) was attached to each entry region of the mixing chamber. All attached tubing had a length of 320cm (4 times 80 cm – a likely length in an actual surgical catheter). Additionally, a hole was drilled through the mixing chamber that was completely independent of the serpentine channel. This channel would be used for guide wire positioning/drainage of the appendage, and was connected to polyurethane tubing with an ID of 4 mm. All tubing described above was attached to Luer Lock male connectors, the most method of connecting delivery syringes to the catheter. This prototype is shown in Figure 6.5 below.

One difference between the prototype and the actual design is the use of multiple, single lumen channels, where an actual device would use a single, multi-lumen tube. For this prototype, the most important variable is channel internal diameter, and maintaining all dimensions as close to 4:1 scale as possible. Due to

time constraints, it was not feasible to have multi-lumen tubing made to custom dimensions. Still, this prototype achieved dimensionally similar internal diameters, confirming its suitability for testing.

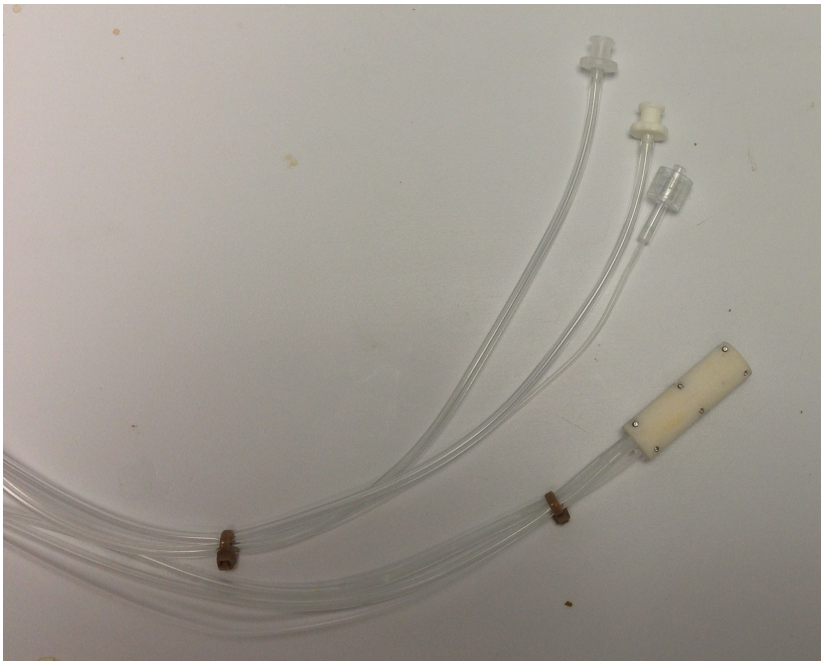

Figure 6.5: Prototype catheter used for fluid transport analysis

In addition, to test the ability to move fluids in and out of the LAA, pig hearts were used for these experiments. Hearts were cut open at the Left Ventricle, and the prototype was inserted into this opening. The prototype traveled through the ventricle into the LAA. Mixed epoxy components would be transported through the prototype, combined in the mixing chamber, and then ejected into the LAA. To ensure this prototype gave an accurate evaluation of the catheter design, parameters for flow rate and fluid properties were the same as described in Table 5.2 in Chapter 5.

In all 6 trials, the prototype catheter was able to mix epoxy components fully, and the epoxy solidified completely in the LAA. For the first 2 trials, however, solidification time was longer than expected, and took 10-12 minutes to fully cure. This is significantly longer than specified complete setting time at room temperature. (~5 minutes) A likely explanation for this was due to temperature, and hearts before these first 2 trials were refrigerated before filling. The epoxy used as a mock filling material is temperature sensitive, and was likely cooled by the pig hearts. For the next four trials, pig hearts were heated in a water bath to 20C before testing with the prototype. These resulted in a much faster setting time.

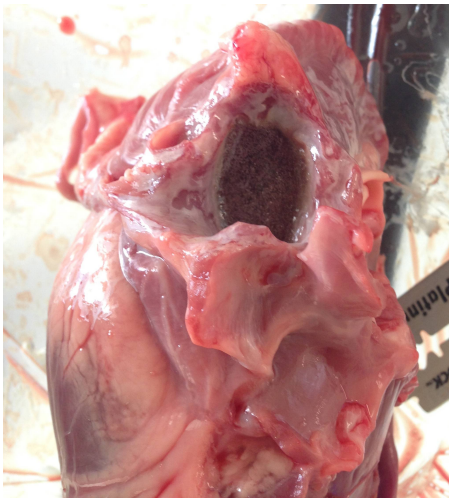

Figure 6.6: Solidified epoxy within the left atrial appendage

Conclusion

The entire catheter device was examined in this chapter. This entailed examining all subfunctions required for a complete occlusion procedure. A Function-Structure diagram was designed to show all interactions and order of subfunctions as well. A dimensionally similar prototype was also built and tested.

This prototype analyzed fluid transport, and showed that filling components can be delivered to a pig heart successfully. Finally, this chapter analyzed manufacturing of a final design that could be used with human patients. Analysis of manufacturing and assembling techniques, as well as FDA regulations for device manufacturing, were analyzed, confirming the current embodiment can be manufactured in a safe and reproducible manner.

Chapter 7: Summary, Conclusions and Future Work

Summary

The aim of this work was to design a device that could better occlude the Left Atrial Appendage than current occlusion methods. This device must have fewer sequelae and offer more complete sealing than currently used physical plugs. Research investigated whether a conforming hydrogel can more effectively occlude the LAA than a physical plug, or other currently used therapies. Additionally, we modeled subfunctions of the device to validate the design, as well as the proposed surgical procedure.

Previous research identified a 2-component hydrogel, comprised of PEG-tetra-thiol and Dextran vinyl sulfone, as a candidate filling material. Experimental work evaluated this material for suitability for this particular application. Measurement of fluid properties of uncured hydrogel components confirmed that the hydrogel could be transported to the LAA through a catheter. Additional experimentation examined material properties of the hydrogel. The hydrogel was shown to swell enough to remain anchored in the appendage. Additionally, the material will degrade slowly, and allow for complete tissue overgrowth of the LAA. All experimentation indicated that the candidate material is suitable for this application, as well as identified optimal material configurations for occlusion.

Additional research examined multiple subfunctions of the surgical procedure. A model was made to examine interactions between a catheter balloon and cardiac tissue. For all chamber openings examined, the catheter balloon was able to form a complete seal around the circumference of the appendage opening, indicating that the device can successfully occlude the appendage under its current embodiment. Another model examined hydrogel component mixing in multiple catheter tip mixing chamber designs. This work identified a mixing chamber design that was quantitatively most effective. Both of these models were also validated experimentally, and experimentation confirmed that the current embodiment could successfully deliver hydrogel to the LAA and solidify it completely.

Future Work

While findings presented in this document indicate that the current embodiment of this device could successfully occlude the LAA, it also demonstrates the importance of further research to continue developing this invention as a treatment method. There are multiple areas that can be investigated further to continue this development.

Further Hydrogel Investigation

Additional research can investigate an optimal material configuration for this application. While experimentation and analysis confirmed its viability for this application, there were some aspects of the material that were not fully examined. Due to material availability, we were unable to investigate how DS number affects

solidification time and volumetric swelling. It is also currently unclear how the addition of non-hydrogel substances, like blood, could affect solidification and material performance. This future work could help determine an optimal material configuration, as well as material modifications that would optimize the surgical procedure.

Additional material experimentation can focus on biocompatibility, and cell adhesion properties of the hydrogel. Previous work from Singh et al. has shown the material to have low toxicity [1j]. However, it is unclear if the material would have strong cell adhesion, and promote endothelial tissue overgrowth. This is a critical component to permanent occlusion, and a cell adhesion assay should be performed to investigate growth rates. It would also be beneficial to look into additives that could increase cell growth rate on this hydrogel.

A final area of material investigation could look into platelet adhesion to the hydrogel, and the risk of clotting as a result of this implant. As mentioned previously, any clotting or thrombus formation in the LAA can cause strokes or other potentially fatal conditions. A better understanding of platelet adhesion, or other methods of clot formation on the filling material, is necessary before concluding the filling material is appropriate for this application.

Balloon Modeling

Balloon modeling could also be investigated further to look at additional LAA opening geometries. While modeling in this study showed a catheter balloon could

occlude typical chamber openings, experimentation showed significant variation in leakage due to variable LAA geometry. Future modeling could look at additional geometries, including asymmetrical ones. Investigation could also look at different balloon sizes, to determine if variations in this area could improve sealing capability. The ultimate goal of this future work would be to determine an optimal balloon configuration that could minimize leakage for a wide range of appendage dimensions and sizes.

Entire System Analysis and Live Animal Trials

A final area of investigation could focus on testing an entire prototype with in-vivo animal trials. Modeling and experimentation presented in this work focused almost exclusively on separate subfunctions of the device. Experimentation also did not look into any long-term biocompatibility or toxicology issues that might arise when using this device in the body. It is of interest to better understand long-term performance of the hydrogel in vivo after the surgical procedure. Along with all other areas of investigation described above, this study would further development of this device, bringing it closer to application of treating symptoms of AF.

Nomenclature

μ	Dynamic viscosity (Pa*s)
ν	Kinematic viscosity (m^2/s)
ρ	Density (kg/m^3)
Φ	Volume fraction (dimensionless)
Φ_m	Maximum volume fraction (dimensionless)
V	Volume of sulute (cm^3)
V	Volume of solvent (cm^3)
$[\eta]$	Intrinsic viscosity (dimensionless)
M	Molecular weight (Da)
K	Mark-Houwink Parameter ($cm^3*mol^{1/2}/g^{3/2}$)
a	Mark-Houwink Parameter (dimensionless)
Q_m	Equilibrium swelling ratio (dimensionless)
V_m	Volumetric swelling ratio (dimensionless)
R_m	Radius multiple (dimensionless)
w	Weight of hydrogel sample (g)
V	Volume of hydrogel sample (g)
E	Elastic modulus (N/m^2)
ν	Poisson ration (dimensionless)
δ_r	Change in hydrogel radius (m)
P_i	Interface pressure between tissue and hydrogel (N/m^2)
R	Radius of hydrogel (m)
r	Outer radius of LAA tissue (m)
L_h	Length of hydrogel plug (m)
μ_f	Coefficient of friction (dimensionless)
P_s	Pressure from syringe (N/m^2)
ω	Polymer mass fraction (dimensionless)
Q	Fluid flow rate ($\mu L/s$)
L	Length of flow channel (m)
Δp	Pressure difference (N/m^2)
D	Diameter of internal channel (m)
t	Time for filling/draining LAA (s)
W	Strain energy
C_{01}, C_{10}	Mooney Rivlin Constants
$\bar{P}_i$	Average interface pressure (N/m^2)

F_I	Interface force (N)
A	Surface area (m^2)
N	Number of data points (dimensionless)
u	Fluid velocity (m/s)
K	Flow consistency index ($Pa*s^n$)
D_{ij}	Diffusion coefficient (cm^2/s)
U	Inlet velocity (m/s)
w	Channel width (mm)
L	Length of channel (mm)
Pe	Peclet Number (dimensionless)
Re	Reynolds number (dimensionless)

Abbreviations

AF	Atrial Fibrillation
DEX	Dextran vinyl sulfone
Dextran	Dextran vinyl sulfone
LA	Left Atrium
LAA	Left Atrial Appendage
LV	Left Ventricle
ME	Mixing Efficiency
PBS	Phosphate buffered saline
PEG	Polyethylene glycol tetra-thiol
STD	Standard deviation
TEA	Triethanolamine
VBN	Viscosity blend number

Sources

Chapter 1: Introduction

[1a] Al-Saady, N. M., Obel, O. A., & Camm, A. J. (1999). Left atrial appendage: structure, function, and role in thromboembolism. *Heart*, *82*(5), 547-554.

[1b] Williams, P. L. (Ed.). (1995). *Gray's anatomy* (Vol. 58). New York: Churchill Livingstone.

[1c] Fuster, Valentin, et al. "ACC/AHA/ESC 2006 Guidelines for the Management of Patients With Atrial Fibrillation—Executive Summary: A Report of the American College of Cardiology/American Heart Association Task Force on Practice Guidelines and the European Society of Cardiology Committee for Practice Guidelines (Writing Committee to Revise the 2001 Guidelines for the Management of Patients With Atrial Fibrillation) Developed in Collaboration With the European Heart Rhythm Association and the Heart Rhythm Society."*Journal of the American College of Cardiology* 48.4 (2006): 854-906.

[1d] Blackshear, J. L., & Odell, J. A. (1996). Appendage obliteration to reduce stroke in cardiac surgical patients with atrial fibrillation. *The Annals of Thoracic Surgery*, *61*(2), 755-759.

[1e] Weisbord, S. D., Whittle, J., & Brooks, R. C. (2001). Is warfarin really underused in patients with atrial fibrillation?. *Journal of general internal medicine*, *16*(11), 743-749.

[1f] Roth, P., Rahimi, A., & Boening, A. (2010). The pericardium-reinforced technique of amputation of the left atrial appendage: Quick, safe, and simple.*The Annals of thoracic surgery*, *90*(1), e11-e13.

[1g] Watchman LAA Closure Technology. (2013). Watchman Technology. Retrieved at http://www.atritech.net/watchman.html

[1h] EP Lab Digest. (2010). LAA Occlusion with Amplatzer Cardiac Plug. Retrieved at http://eplabdigest.com/articles/Left-Atrial-Appendage-Occlusion-with-Amplatzer-Cardiac-Plug

[1i] Hiemstra, C., van der Aa, L. J., Zhong, Z., Dijkstra, P. J., & Feijen, J. (2007). Novel in situ forming, degradable dextran hydrogels by Michael addition chemistry: synthesis, rheology, and degradation. *Macromolecules*, *40*(4), 1165-1173.

[1j] Singh, A., Suri, S., & Roy, K. (2009). < i> In-situ</i> crosslinking hydrogels for combinatorial delivery of chemokines and siRNA–DNA carrying microparticles to dendritic cells. *Biomaterials*, *30*(28), 5187-5200.

[1k] Lesh, M. D., & van der Burg, E. J. (2000). *U.S. Patent No. 6,152,144*. Washington, DC: U.S. Patent and Trademark Office.

Chapter 2: Material Testing

[2a] Bird, R. B., Stewart, W. E., & Lightfoot, E. N. (2006). *Transport phenomena*. Wiley.

[2b] Sigma Aldrich. (2013). Polyethylene Glycol. Retrieved from http://www.sigmaaldrich.com/catalog/product/aldrich/309028?lang=en&region=US

[2c] Fitzgibbons, J. F., Koler, R. D., & Jones, R. T. (1976). Red cell age-related changes of hemoglobins AIa+ b and AIc in normal and diabetic subjects.*Journal of Clinical Investigation*, *58*(4), 820.

[2d] Hiemenz, P. C. (1984). *Polymer chemistry: the basic concepts*. CRC press.

[2e] Godbey, W. T., Wu, K. K., & Mikos, A. G. (1999). Size matters: molecular weight affects the efficiency of poly (ethyleneimine) as a gene delivery vehicle.*Journal of biomedical materials research*, *45*(3), 268-275.

[2f] Charalambous, G., Inglett, G. (1983). Instrumental Analysis of Food. Elsevier, Chap. 9.

[2g] Americal Polymer Standards Corporation. (2013). Mark Houwink Parameters for Polymers: Retrieved at http://www.ampolymer.com/a%20&%20K.html

[2h] Hamrock, B. J., Jacobson, B. O., Schmid, S. R., Jacobson, B., & Jacobson, B. (1999). *Fundamentals of machine elements* (pp. 290-292). Singapore: WCB/McGraw-Hill.

[2i] Park, Y. D., Tirelli, N., & Hubbell, J. A. (2003). Photopolymerized hyaluronic acid-based hydrogels and interpenetrating networks. *Biomaterials*, *24*(6), 893-900

[2j] Moriwaki, T., Oie, T., Takamizawa, K., Murayama, Y., Fukuda, T., Omata, S., ... & Nakayama, Y. (2011). Variations in local elastic modulus along the length of the aorta as observed by use of a scanning haptic microscope (SHM).*Journal of Artificial Organs*, *14*(4), 276-283.

[2k] Chen, L., Zhang, D., & Zhang, J. (2009). The appraisal of mechanical properties and friction coefficient of PVA hydro-gel]. *Sheng wu yi xue gong cheng xue za zhi= Journal of biomedical engineering= Shengwu yixue gongchengxue zazhi*, *26*(5), 1021.

[2l] Heist, E. K., Refaat, M., Danik, S. B., Holmvang, G., Ruskin, J. N., & Mansour, M. (2006). Analysis of the left atrial appendage by magnetic resonance angiography in patients with atrial fibrillation. *Heart Rhythm*, *3*(11), 1313-1318.

Chapter 3: Fluid Transport Analysis

[3a] Radwin, R. G., Oh, S., Jensen, T. R., & Webster, J. G. (1992). External finger forces in submaximal five-finger static pinch prehension. *Ergonomics*, *35*(3), 275-288.

[3b] http://www.lctglobalinc.com/pdf/catalog/id_24.pdf

[3c] Merrill, E. W. (1969). Rheology of blood. *Physiol. Rev*, *49*(4), 863-888.

[3d] Gonzalez-Tello, P., Camacho, F., & Blazquez, G. (1994). Density and viscosity of concentrated aqueous solutions of polyethylene glycol. *Journal of Chemical and Engineering Data*, *39*(3), 611-614.

[3e] Maples, R. E. (2000). *Petroleum refinery process economics*. PennWell Books.

[3f]Fox, R. W., McDonald, A. T., & Pritchard, P. J. (1998). *Introduction to fluid mechanics* (Vol. 2). New York: John Wiley & Sons.

[3g] Stephenson, D. J. (1989). *Pipeline design for water engineers* (Vol. 40). Elsevier Science.

[3h] Beinart, R., Heist, E. K., Newell, J. B., Holmvang G., Ruskin, J. N., & Mandour, M. (2011). Left atrial appendage dimensions predict the risk of stroke/TIA in patients with atrial fibrillation. *Journal of Cardiovascular Electrophysiology*, *22*(1), 10-15.

Chapter 4: Balloon Isolation Modeling

[4a] De Beule, M., Mortier, P., Carlier, S. G., Verhegghe, B., Van Impe, R., & Verdonck, P. (2008). Realistic finite element-based stent design: the impact of balloon folding. *Journal of biomechanics*, *41*(2), 383-389.

[4b] Heist, E. K., Refaat, M., Danik, S. B., Holmvang, G., Ruskin, J. N., & Mansour, M. (2006). Analysis of the left atrial appendage by magnetic resonance angiography in patients with atrial fibrillation. *Heart Rhythm*, *3*(11), 1313-1318.

[4c] BRAUNWALD, E., & AWE, W. C. (1963). The syndrome of severe mitral regurgitation with normal left atrial pressure. *Circulation*, *27*(1), 29-35.

[4d] David Chua, S. N., MacDonald, B. J., & Hashmi, M. S. J. (2004). Finite element simulation of slotted tube (stent) with the presence of plaque and artery by balloon expansion. *Journal of materials processing technology*, *155*, 1772-1779.

[4e] David Chua, S. N., Mac Donald, B. J., & Hashmi, M. S. J. (2003). Finite element simulation of stent and balloon interaction. *Journal of Materials Processing Technology*, *143*, 591-597.

[4f] Bower, A. F. (2011). *Applied mechanics of solids*. CRC press.

[4g] Moriwaki, T., Oie, T., Takamizawa, K., Murayama, Y., Fukuda, T., Omata, S., ... & Nakayama, Y. (2011). Variations in local elastic modulus along the length of the aorta as observed by use of a scanning haptic microscope (SHM).*Journal of Artificial Organs*, *14*(4), 276-283.

[4h] Braunwald, E., & Awe, W. C. (1963). The syndrome of severe mitral regurgitation with normal left atrial pressure. *Circulation*, *27*(1), 29-35.

Chapter 5: Hydrogel Mixing Analysis

[5a] Stroock, A. D., Dertinger, S. K., Ajdari, A., Mezić, I., Stone, H. A., & Whitesides, G. M. (2002). Chaotic mixer for microchannels. *Science*,*295*(5555), 647-651.

[5b] Nguyen, N. T. (2011). *Micromixers: fundamentals, design and fabrication.* William Andrew.

[5c] Nguyen, Q. H., & Choi, S. B. (2012). Optimal Design Methodology of Magnetorheological Fluid Based Mechanisms.

[5d] R. Bird, W. Stewart, E. Lightfoot, *Transport Phenomena*, Wiley, New York (2007).

[5e] Gonzalez-Tello, P., Camacho, F., & Blazquez, G. (1994). Density and viscosity of concentrated aqueous solutions of polyethylene glycol. *Journal of Chemical and Engineering Data*, *39*(3), 611-614.

[5f] Vignes, A. (1967). Predictive Theory for Multicomponent Diffusion Coefficients. *Industrial & Engineering Chemistry Fundamentals*, *6*(4), 614-616

[5g] Rehfeldt, S., & Stichlmair, J. (2007). Measurement and calculation of multicomponent diffusion coefficients in liquids. *Fluid phase equilibria*, *256*(1), 99-104

[5h] Chin, K. P., Li, S. F., Yao, Y. J., & Yue, L. S. (1991). Infinite dilution diffusion coefficients of poly (ethylene glycol) and poly (propylene glycol) in water in the temperature range 303-318 K. *Journal of Chemical and Engineering Data*, *36*(3), 329-331.

[5i] Vergara, A., Annunziata, O., Paduano, L., Miller, D. G., Albright, J. G., & Sartorio, R. (2004). Multicomponent diffusion in crowded solutions. 2. Mutual diffusion in the ternary system tetra (ethylene glycol)-NaCl-water. *The Journal of Physical Chemistry B*, *108*(8), 2764-2772.

[5j] Trampel, R., Schiller, J., Naji, L., Stallmach, F., Kärger, J., & Arnold, K. (2002). Self-diffusion of polymers in cartilage as studied by pulsed field gradient NMR.*Biophysical chemistry*, *97*(2),

[5k] R. Taylor and R. Krishna, *Multicomponent Mass Transfer*, Wiley, New York (1993).

[5l] Zhang, X. (2006). Study of epoxy toughening in bulk and disbond initiation at epoxy/aluminum interfaces.

Chapter 6: Entire System Analysis

[6a] Otto, K. N., & Wood, K. L. (2001). Product design: techniques in reverse engineering and new product development.

[6b] BMC. (2005). BMC's Multi-lumen Profile Extrusions. Retrieved at http://home.earthlink.net/~bmc-medical-extrusions/

[6c] Covidien. (2012). MAHURKAR™* 12Fr. Triple Lumen Straight and Curved Extension Catheters. Retrieved at http://www.kendallhealthcare.com/kendallhealthcare/pageBuilder.aspx?contentID=108700&webPageID=0&topicID=74273&breadcrumbs=0:121623,81037:0,69932:0

[6d] Boothroyd, G., Dewhurst, P., & Knight, W. A. (2010). *Product design for manufacture and assembly* (Vol. 74). CRC Press.

[6e] US Food and Drug Administration. (2013). CFR 21 814.20. Retrieved at http://www.accessdata.fda.gov/scripts/cdrh/cfdocs/cfcfr/CFRSearch.cfm?CFRPart=820&showFR=1

[6f] US Food and Drug Administration. (2013). CFR 21 820. Retrieved at http://www.accessdata.fda.gov/scripts/cdrh/cfdocs/cfcfr/CFRSearch.cfm?CFRPart=820&showFR=1

Vita

Andrew Zimbroff attended high school at The Webb Schools in Claremont, CA. In 2008, he enrolled at Stanford University, receiving the degree of Bachelors of Science in Mechanical Engineering in 2008, and Master of Science in Mechanical Engineering in 2009.

Andrew's other interests include entrepreneurship, commercialization of technology, sports, and travel.

Permanent Contact Information:
azimbroff@gmail.com

This dissertation was typed by the author